Materials Science Forum
ISSN: 1662-9752, Vol. 962, pp 82-88
doi:10.4028/www.scientific.net/MSF.962.82

Submitted: 2018-12-06
Accepted: 2018-12-17
Online: 2019-07-12

Effect of SnO_2 Nanoparticle Doping on Structural, Morphological and Thermal Properties of PVA-PVP Polymer Blend

B Guruswamy[1], V Ravindrachary[1]*, C Shruthi[1], Mylarappa M[2]

[1]Department of Physics, Mangalore University, Mangalagangotri-574199, India

[2]Research centre Dept. of Chemistry, AMC Engineering College, Bangalore-560083, India.

*Email: vravi2000@yahoo.com

Keywords: PVA-PVP Polymer blend, SnO_2 Nanoparticles, XRD, SEM, AFM, DSC

Abstract: The n-type semiconductor SnO_2 nanoparticles were synthesised using standard route and the effect of this nanoparticle doping on structural, morphological and thermal properties of PVA-PVP polymer blend has been investigated. Pure and PVA-PVP/SnO_2 Nanocomposite films were prepared using solution casting technique. The powder X-ray diffraction result shows that the crystalline nature of the blend increases with doping level. FESEM study shows that the surface morphology of the polymer nanocomposite varies with doping level. AFM study reveals that in the nano-composite films, the average roughness changes with dopant concentration. The DSC studies on the samples were performed from 40°C to 400°C under nitrogen atmosphere and it shows that the thermal properties of the blend changes with doping concentration.

Introduction

In recent years the doped/blended polymers have attracted the scientific and technological researchers due to utilities in all fields. Here it is well known that the desired property of a polymer for a specific application can be achieved through blending and doping. Here the polymer blending is considered to be one of the most important and modern way of developing new polymeric materials with a wide variety of physical and chemical properties. The major advantage of polymer blending is that the properties of a final product can be tailored suitably for specific application as these blend properties are mainly depends on the characteristics of the parent homo polymers and the composition. Doping a polymer is another way of tailoring the physical and chemical properties of polymer for specific applications. Here the change in the property of the polymer upon doping is mainly depends on the type of the polymer, chemical nature and size of the dopant and the way in which the dopant interacts with the host polymer. Particularly the nanoparticle doped polymers are attracted much attention due to the various potential applications including sensor properties. Here the combination of inorganic nanoparticles and an organic polymer provides a simple route to stable and processable composite materials, which integrating the promising properties of both components of polymer and dopant [1-4].

Poly vinyl Pyrrolidone (PVP) is an amorphous polymer which is hygroscopic in nature and it attains complex formation ability, environmentally stable, easy processability, modest electrical conductivity, and more charge transport mechanism, these chemical structures induces extreme changes in electronic properties. Poly vinyl alcohol (PVA) is another superior polymerwith semi crystalline nature having some interesting properties such as water soluble, synthetic and biocompatible non toxic, odourless, film formation ability and adhesive nature which are very much essential for various applications in biomedical field. When PVA/PVP blend is formed, the interactions between the carbonyl group of PVP and the hydroxyl group of PVA takes place through the intermolecular hydrogen bonding which results in the formation of new structure.When such a blend is doped with metal oxide nanoparticles, microstructure and other macroscopic properties of the blend are altogether different from parent properties of the film. These films are useful in the field of electronic devices such as liquid crystal displays, photovoltaic devices including high energy

electrochemical deviceslike Batteries, and fuel cells but the foremost advantage is found to be its sensor application [4-6]. Keeping in view the above applications, the present work aims to prepare SnO_2 nano-particles and dope these into PVA-PVP blends in order to obtain suitable films for prospective structural, morphological and thermal applications.

Experimental

The PVA were obtained in powder form from M/s. S. D. fine-Chem. Ltd, Mumbai. PVP, $SnCl_2\,2H_2O$ from M/s. Loba Chemie Pvt. Ltd. Mumbai. SnO_2 nanoparticles were synthesized through a chemical precipitation method using $SnCl_2 2H_2O$ [3] .The pure and SnO_2 doped PVA-PVP composite films were prepared by solution casting method [1, 3]. The XRD studies were carried out using RIGAKU Miniflex-600 benchtop X-ray diffractometer and morphology study using FESEM with Carl Zeiss instrument. AFM analyses were carried out using NANOSURF EZ2-Flux Atomic Force Microscope. Universal (SDT Q600) TG/DTA instrument is used to measure the DSC. In this instrument the thermal analysis of the samples were performed from 40°C to 400°C with a heating rate of 10°C/min under nitrogen atmosphere (flowing rate 100 ml/min)

Structural Study (X-Ray Diffraction)

Fig. 1 shows the observed X-ray diffraction patrons of pure PVA-PVP blend and the blends doped with different concentrations of SnO_2 as dopant. Form the figure it is clear that for pure PVA-PVP blend a broad peak centered at $2\theta = 19.65°$ is observed which indicates the semi crystalline nature of the polymer blend.

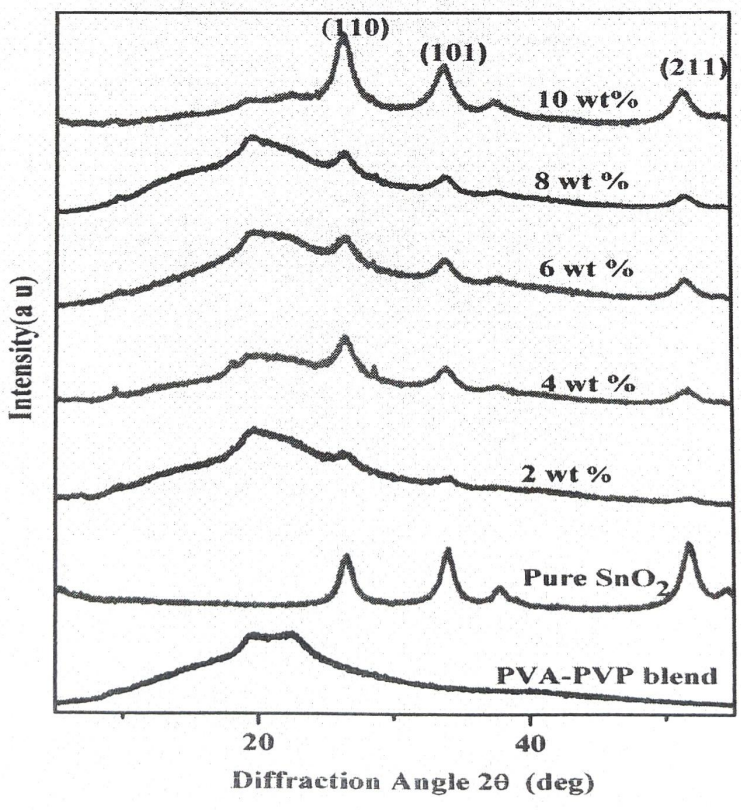

Fig. 1 X-ray diffraction scans of pure PVA/PVP blend and PVA-PVP/SnO_2 Nanocomposites

Here the crystalline phase may be regarded as amorphous phase with small crystallites which are distributed randomly. For pure SnO_2 the well-defined diffraction peaks are appeared at 25°, 33° and 51° that show the crystalline nature of the nanoparticles [3]. For the composite films the crystalline peaks are observed at 25.91°, 33.77° and 51.64° which are nothing but the modified peaks of pure

SnO_2 nanoparticles. Using the observed XRD data crystallinity of the films were determined and the results are given in Table 1. From the table it is clear that the crystallinity/structural ordering of the nanocomposite increases with increase in doping level. This is shows that the dopant interacts with the blend via inter/intra molecularly leads to ordering of the molecules [1, 5]. These interactions or ordering of the molecule increases with doping level which implied increase in the degree of crystallization. Here it is clear that SnO_2 nano particles are retain their crystal structure along with complex formation.

Table.1 XRD results of pure blend and PVA-PVP/SnO_2 nanocomposites

Doping level M(wt%)	**Crystallinity X_c(%)**
Pure blend	20.57
2wt%	32.44
4wt%	42.20
6wt%	50.23
8wt%	58.35
10wt%	65.14

Morphological Study (FESEM Analysis)

The surface morphology of pure blend and PVA-PVP/SnO_2 Nanocomposite films were analysed using FESEM micrographs. The Fig 2 (a) shows the pure SnO_2 Nano -particles and 2 (b) shows the pure PVA-PVP blend and 2 (c), 2 (d) shows the 2wt%, 10wt% SnO_2 doped Nanocomposite films. From the Fig 2 (a) it is clear that the pure SnO_2 nanoparticles are spherical in shape and of 100nm in size. For pure blend (Fig 2 (b)) it is observed that the prepared blend films are transparent, homogeneous and uniform surface morphology. This feature reveals the smooth surface with miscibility may be due to interaction of PVA and carbonyl group of PVP [5-7]. After adding SnO_2 to the blend matrix (2wt% Fig 2 (c)), the SnO_2 particles are freely distributed on the surface of the composite film as a result blend surface becomes rough. This shows that the SnO_2 nanoparticles were fully dispersed–well within the polymeric blend matrix. From the Fig 2 (d) (10wt %) confirms that the segregation of the nanoparticles takes place along with change in surface morphology. That means the degree of roughness of the composite films increases with increasing the SnO_2 wt%. Here the segregation of the nano-paticles in the host matrix along with the interaction and complexations between the nanoparticles and PVA-PVP polymer blend. From the observed FESEM images it is clear that the doping changes the microstructure of pristine polymer blend and composite films.

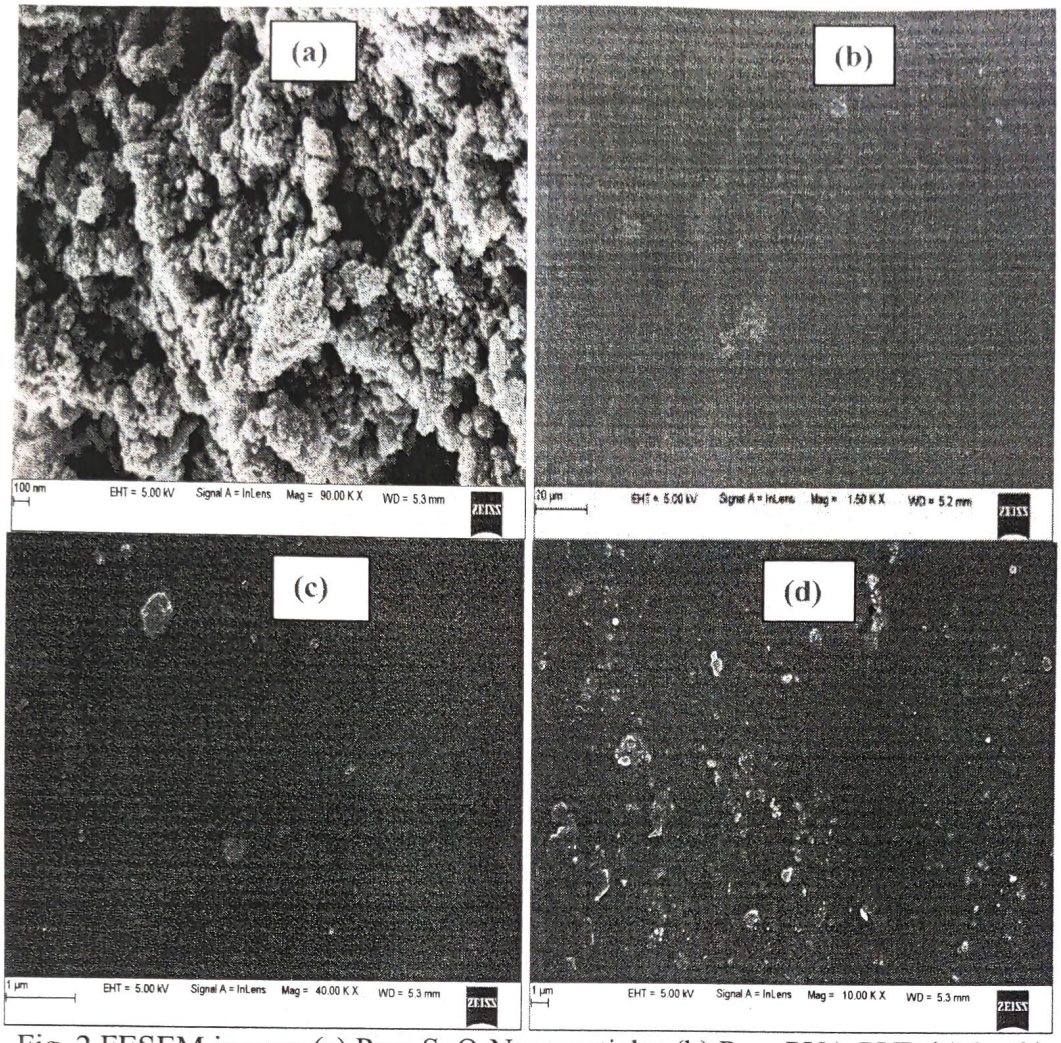

Fig. 2 FESEM images (a) Pure SnO_2Nanoparticles (b) Pure PVA-PVP (c) 2wt% of PVA-PVP/SnO_2 (d) 10 wt% PVA-PVP/SnO_2

AFM study

The outer surface modification of polymer films was studied by atomic force microscopy (AFM). Fig 3 (a-d) shows the semi-contact mode images by AFM for pure PVA-PVP blend and SnO_2 doped composite films with a scan size (5 × 5μm) and (10 × 10μm) both 2D and 3D images. Average roughness data taken from the images gives three parameters such as Root mean Squared (RMS) Roughness, arithmetic mean (Ra) and the ration of the image surface area to the image projected surface area(r) which are mentioned in the below Table 2. It is observed from the image (Fig.3 (a, b)) that pure PVA-PVP blend shows smooth surface and small amount of crystallization hence it is a semicrystlline [7] in nature which supports XRD studies. In the composite films the result shows that the surface is modified upon doping and roughness increases with doping. Fig. 3 (c,) also shows the bright regions, cluster formation and spike (needle-like) structures that are represents the added SnO_2 dopant. Here the SnO_2 nanoparticles are randomly distributed throughout the PVA-PVP blend. Different surface morphology is observed at each dopant wt% level which confirms the interaction between polymer and dopant. As a result compared to pure films both in 2D and 3D images, more surface roughness is observed in the composite films.

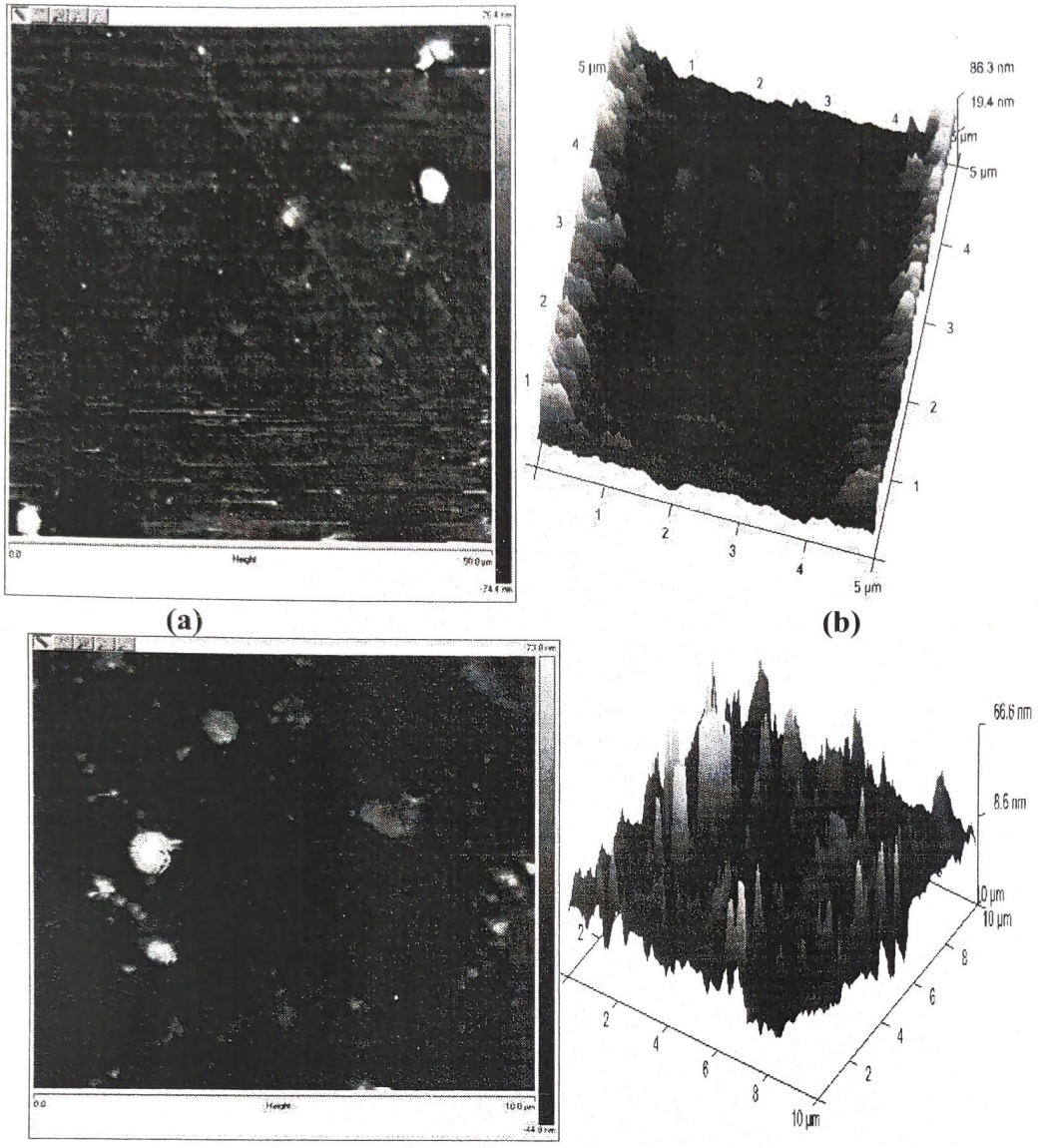

Fig. 3 AFM images of(a) Pure PVA-PVP 2D images (b) Pure PVA-PVP 3D images (c) 10w t% of PVA-PVP/SnO_2 2D images (d) 10 wt% PVA-PVP/SnO_2 3D images

Table.2 Average roughness data taken from AFM images three parameters are presented, root mean squared (RMS), arithmetic mean (Ra), and the ratio of the image surface area to the image projected surface (r)

	RMS Roughness(nm)	**Ra Roughness(nm)**	**r Rouhness (µm/µm)**
Pure blend	8.62± 2.85	4.94± 3.62	1.05±0.02
10wt% composite	15.6± 2.45	8.68± 1.52	1.02 ±0.01

DSC Studies

The thermal properties of the pure blend and PVA-PVP/SnO_2 nanocomposite were analysis by the DSC and the obtained results are shown in Fig 4 and the other thermal properties like glass transitions temperatures (T_g) and melting temperatures (T_m) relaxation temperature (T_α), Thermal decomposition temperature (T_d) are in Table 3.

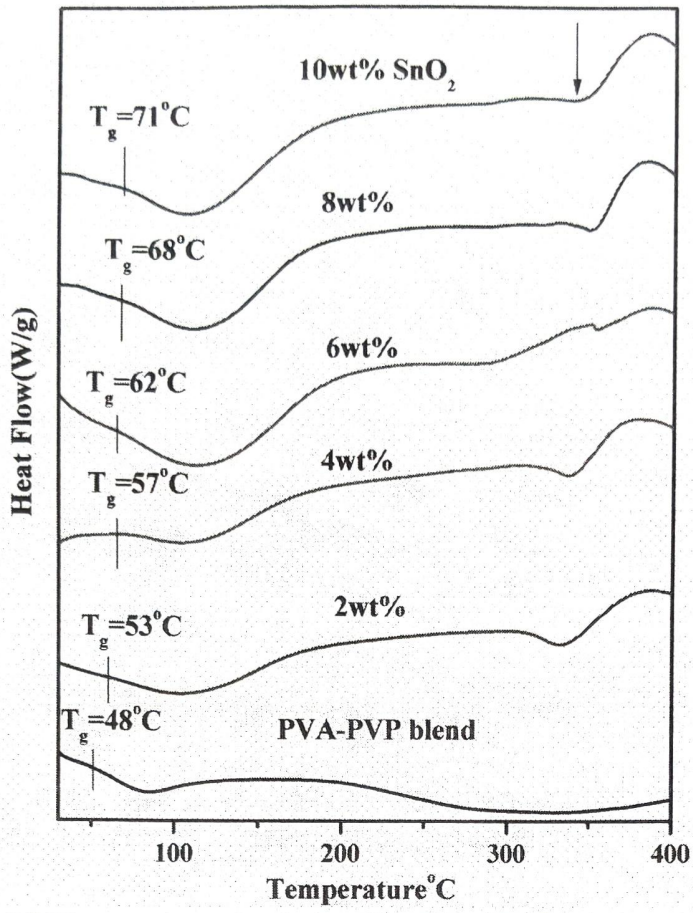

Fig. 4 The DSC Thermogram of pure blend& PVA-PVP /SnO_2 nanocomposites

From the figure it is observed that the DSC thermogram of all samples exhibits the single transition temperature (T_g) (for pure its value is 48°C) indicating the complete miscibility of PVA and PVP. Here the relaxation process resulting from micro-Brownian motion of the main chain backbone which is [6,7] a broad transition may be assigned to the –relaxation (T_α) and its value is observed at77°C for pure blend. Similarly T_m is observed around 321°C and the T_d around 370°C for pure blend.

For the doped blend it is observed from the Table 3 that the Tg increases with increase in dopant concentration and shows maximum of 71 °C, similarly Tα from77°C to 108 °C. The dopant also affects the Tm and Td, Tm varies from 321°C to 351°C and Td from 370°C to 385°C.The increase in Tg with dopant concentration is the direct evidence of the interaction between blend polymer matrix and dopant. From XRD and AFM studies it is evident that the crystallinity of the blend increases with the doping level. Usually in these crystalline regions the segmental mobility of the blend chain reduce. Hence increase in crystalline region upon the addition of SnO_2 affects the segmental motion and segments become more rigid as dopant level increases. This feature is also observed from the broadening of the width of α-relaxation which associated with crystalline region and the enthalpy associated with this endothermic peak increase with increasing SnO_2 dopant. Hence the polymer blend matrix become more and more rigid upon addition of dopant as a result Tα as well as Tg increases with doping level. The shift of Td is towards the higher from 370 °C to 385°C confirms the behavior of the dopant as plasticizer and indicates the formation of an intermolecular interaction between the polymer blend and the nanoparticles. The presence of an interaction was confirmed by X-ray, and SEM analysis.

Table 3 DSC results: glass transition temperature (Tg), α-relaxation temperature (Tα), melting temperatures (Tm) and degradation temperature (Td)) of pure PVA-PVP blend and PVA-PVP/ SnO_2 nano-composite

.Doping (wt %)	T_g (°C)	T_α (°C)	T_m (°C)	T_d (°C)
Pure blend	48	77	321	370
2	53	99	330	373
4	57	102	334	376
6	62	104	338	381
8	68	106	341	383
10	71	108	351	385

Conclusions

The n-type semiconductor SnO_2 nanoparticles were synthesized using standard methods, and the effect of these SnO_2 Nanoparticles doping on structural, Morphological and thermal properties of the PVA-PVP polymer blend was studied. From these studies, the above results are more evident to the formation of doped SnO_2 nanoparticles interpenetrating polymer chains of PVA-PVP blend polymer network which improves the structural, morphological and thermal properties of the blend nanocomposites.

Acknowledgments

The authors are grateful to PURSE lab Mangalore University, Mangalagangothri, innovation centre MIT Manipal for providing the instrumental facility

References

[1] V Ravindrachary, R F Bhajantri, A Harish, Ismayil, and C Ranganathaiah: *Phys. Status Solidi C,* 6 No 11 (2009) 2438-2441.

[2] B Guruswamy, V Ravindrachary, C Shruthi, Shreedatta Hegde, Rohan N Sagar, S D Praveena : *Indian Journal of Advances In Chemical Science,* Vol 6, No 1 2018 17-20

[3] L N Moghadam, A E B Karimabad, M S Niasari, H Safardoust: *Journal of Nanostructures* 5 (2015) 47-53

[4] E M Abdelrazek , I S Elashmami, A El-khodary, A Yassin: *Current Applied Physics* 10 (2010) 607-613

[5] S Mallakpour, A Jarahiyan : *Polymer-Plastic Technology and Engineering,* Vol 56, No.10 (2017) 1059-1067

[6] I S Elashmawi, H E A Baieth : *Current Applied Physics,* 12 (2012) 141-146

[7] B M Baraker, B Lobo: *Indian Journal of Pure & Applied Physics* 54 (2016) 634-640

Open Access

SCHOLARENA

Journal of Waste Management and Disposal

RESEARCH ARTICLE

ISSN: 2641-8827

Recycling and Reusing of Li_2CO_3 and $Co(OH)_2$ from Waste Lithium ion Batteries for Energy Storage and Thermal Studies

Mylarappa M[1,2*], Venkata Lakshmi V[1] and Kantharaju S[3]

[1]Research centre, Department of Chemistry, AMC Engineering College, Bengaluru, Karnataka, India
[2]Department of Studies and Research in Chemistry, B.H Road, Tumkur University, Karnataka, India
[3]Department of Chemistry, Sri Jagadguru Renukacharya College of Science, Arts and Commerce Bengaluru, Karnataka, India

*Corresponding author: Mylarappa M, Research centre, Department of Chemistry, AMC Engineering College, Bengaluru-560083, Karnataka, India; Department of Studies and Research in Chemistry, B.H Road, Tumkur University Tumkur-572103, Karnataka, India, Tel: +919742413751, Email: mylu4mkallihatti@gmail.com

Citation: Mylarappa M, Venkata Lakshmi V, Kantharaju S (2019) Recycling and Reusing of Li_2CO_3 and $Co(OH)_2$ from Waste Lithium ion Batteries for Energy Storage and Thermal Studies. J Waste Manag Disposal 2: 301

Article history: Received: 12 July 2019, **Accepted:** 09 September 2019, **Published:** 11 September 2019

Abstract

The present study is revealed the recycling and reusing of Li_2CO_3 and $Co(OH)_2$ obtained from waste lithium ion batteries using eco-friendly leaching materials (oxalic acid and citric acid) and their energy storage and thermal properties were studied. The oxidation states, composition and chemical formula of elements in the dry powder were analyzed using X- ray photoelectron spectroscopy (XPS). The particle size and surface morphologies were done by using X-ray diffraction (XRD) and Scanning Electron Microscopy (SEM). The Energy Dispersive X-Ray analysis (EDAX) and Fourier Transform Infrared Spectrometer (FTIR) were employed to know the chemical constituents and functional groups identification in the samples. The obtained Li_2CO_3 and $Co(OH)_2$ particles from waste batteries were further used to study their energy storage and thermal properties.

Keywords: Waste LIB's; Li_2CO_3; $Co(OH)_2$; Energy storage; Thermal Studies

List of abbreviations: LIBs: Li-Ion Batteries; EDAX: Energy-Dispersive X-Ray Spectrometer; OA: Oxalic Acid; CA: Citric Acid; SEM: Scanning Electron Microscopy; FTIR: Fourier Transform Infrared Spectroscopy; XRD: X-Ray Diffraction Analysis; XPS: X-Ray Photoelectron Spectroscopy; CV: Cyclic Voltammetry; EIS: Electrochemical Impedance Spectroscopy; Rct: Charge Transfer Resistance; Cdl: Double-Layer Capacitance; NMP: N-Methyl-2-Pyrrolidone; PVDF: Polyvinylidene Fluoride; ICP-OES: Inductive Coupled Plasma-Optical Emission Spectrometry; TGA: Thermal Gravimetric Analysis; DSC: Differential Scanning Calorimeter; DTA: Differential Thermal Analysis; PTFE: Polytetrafluoroethylene; SF: Stacking Fault; ε: Strain; δ: Dislocation Density; FWHM: Full Width At Half Maximum; HF: Hydrogen Fluoride; Tg: Glass Transition Temperature; GCD: Galvanostatic Charge-Discharge; ΔV: Potential Window; Ip: Peak Current; D: Diffusion Co-Efficient; W: Warburg Impedance; A: Active Surface Area; EO: Oxidation potential; ER: reduction potential; Δt: Discharge time; Cs: Specific Capacitance; E: Energy Density; P: Power Density

Introduction

Nowadays, it is necessary to minimize the utilization of batteries such as Li-ion, Ni-Cadmium, lead acid and alkaline type of batteries and these batteries contains hazardous metals (Li, Co, Ni, Cd, and Zn, Mn). The Li-ion batteries (LIB's) are the electronic wastes have developed quickly due to operation of new techniques in electronic devices and energy storage devices [1-3].

The usage of these batteries in day to day life increases at worldwide. The LIBs are used as power sources in mobile telephone, cameras, computers and other modern life purposes due to their light weight, high voltage, small self-discharge rates, good performance and high energy density [4-7]. On the other hand, the waste LIB's are not only containing valuable metal but also produce large amounts of metal-containing hazardous waste to the soil, air and water sources in the environment [8]. Moreover, when comes in contact with the industrial waste and sewage, it percolates into the soil to water bodies [9-10].

Discarded Li-ion batteries are defined as hazardous waste by every county and causes severe damage to the environment and public health [11]. On the other hand waste batteries contain valuable metals like Co, Li, Mn and Ni [12]. In this regard, the recycling and re-use of Li and Co from waste Li-ion batteries can take enormous economic profits, environmental protection and resource conservation. Hence, development of recycling technologies for spent LIB's has attracted great attention, both for environmental protection and resource conservation [13]. The recovery as well as recycling of Li and Co from the waste batteries will not only

preserve the natural resources but will also decreases environmental problems. The recovery steps involve sequence of separation and purification of Li, Co and other constituents which may yield the secondary contamination. Hence, it is essential and needed to change simple, profitable.

Different experimental procedure for recovery of Li and Co from waste LIB's have been described using pyrometallurgical, bio-metallurgical and hydrometallurgical methods [14]. In the recovery of Li and Co from pyrometallurgical, the binder, release of harmful gases and organic electrolyte were burnt off and also Li and Al are vanished in the slag due to high energy consumption. The bio-hydrometallurgical processes have some benefits such as higher productivity, low cost but the handling period is long and the necessary microorganisms are hard to incubate efficiently [15].

Therefore, hydrometallurgical processes exhibit an alternative method to turn waste batteries in to pure metals/metal salts with a low energy, cost and less toxic gases. The hydrometallurgical methods are deliberated appropriate because of the benefits such as high yield of metals, pureness and nominal air emission. Acid leaching is a significant method for recovering metals and it brings metals into solution, helped at times by a reducing agent that converts the metal to a more soluble oxidation state. The presence of metal ions in the aqueous phase is definitely separated by precipitation, electrochemical and solvent extraction techniques [16-18].

Many leaching methods were done using inorganic acid as leaching agents like H_2SO_4 [19], HCl and HNO_3 [20-21]. In hydrometal lurgical methods, the recovery of metals from battery waste the use of H_2SO_4 was described as matched to other acids and the H_2SO_4 is less harmful to the surroundings [22]. We are selecting low- environmental-impact recovery process using oxalic acid ($H_2C_2O_4$) and citric acid ($C_6H_8O_7$) as leachants to recover Li and Co from waste LIB's. The two acids were selected because of their easy natural degradation and the absence of toxic gases in the leaching process and these two acids were superior leachants to H_2SO_4.

The main significance of oxalic acid and citric acid in the soil pore water results greater solubility and the formation of compounds of oxalic acid and citric acid with the soil salts result in the improvement of the absorption of nutrients by plants [23]. Due to the complexation action of OA and CA, they have ability to supply protons to the soil solution [24] and from the formation of soluble cation-organic acid complexes, which delivers a straight route for absorption [25-27]. Even though these chelating combinations mobilize the soil heavy metals and also purify a soil via soil washing experiments.

According to literature, several main techniques have already been investigated to recover metals from waste LIBs as indicated in Table 1.

References	Sample	Condition	Method
Y. Shen, *et al.* [28]	Co, Ni	6M HCl 95 °C,	Hydrometallurgical
Y. Pranolo, *et al.* [29]	Co,Li,	H_2SO_4 40 °C,	Solvent Extraction
K. Provazi, *et al.* [30]	Mixed	H_2SO_4,100 °C,	Precipitation
J.M. Zhao, *et al.* [31]	LIBs	Cyanex 272	Solvent Extraction
S. Castillo, *et al.* [32]	LIBs	HNO_3, HCl,80 °C	Precipitation
Contestabile, *et al.* [33]	$LiCoO_2$	4M HCl, 80 °C	Laboratory Process
Jingu Kang, *et al.* [34]	Co,Li, Ni	2M H_2SO_4 ,0 °C,	Solvent Extraction
Wang *et al.* [35]	Co, Li	4M HCl, 80 °C,	Hydrometallurgical
G. Dorella *et al.* [36]	Co, Li,	H_2SO_4, 80 °C,	Liq-Liq Extraction
J. Li, *et al.* [37]	Co.Li, Ni	4M HCl, 80 °C,	Precipitation
L. Chen, *et al.* [38]	CoC_2O_4	4 M H_2SO_4,85 °C	Hydrometallurgical
C. Lupi, et al. [39]	Ni, Co	pH 3-3.2, 50 °C	Hydrometallurgical
Badawy, *et al.* [40]	Co	4M HCl, 80 °C	Precipitation
D. Mishra, *et al.* [41]	Co,Li	ferrooxidans	Bioleaching
P. Zhang, *et al.* [42]	Co,Li	4M HCl, 80 °C	Hydrometallurgical
Li Li, *et al.* [43]	Co,Li	Citric acid, 90 °C	Hydrometallurgical
S.M Shin, *et al.* [44]	Co,Li	H_2SO_4, 75 °C.	Hydrometallurgical
Mantuano, *et al.* [45]	Co, Li	H_2SO_4, Cyanex	Hydrometallurgical
B. Xin, *et al.* [46]	Co,Li	ferrooxidans	Bioleaching
K.K. Yoo, *et al.* [47]	LIBs	ferrooxidans	Bioleaching
M.S. Sonmez, *et al.* [48]	(Pb-Acid)	Citric acid, 20 °C	Pb citrate synthesis

Table 1: Separation and recovery methods studied by several earlie references

The recycling and re-use of Li_2CO_3 and $Co(OH)_2$ from waste LIB's using environment friendly materials by hydrometallurgical method and their characterizations, cyclic voltammetry (CV), electrochemical impedance spectra (EIS), Galvanostatic charge-discharge and thermal analysis have not yet been reported. The present research work is focus on the recovery of Li_2CO_3 and $Co(OH)_2$ obtained

from battery leach solution using eco-friendly materials (oxalic acid and citric acid) by hydrometallurgical process. From the battery leached solution, prepared nano sized Li_2CO_3 and $Co(OH)_2$ nano particles. The recoverd Li_2CO_3 and $Co(OH)_2$ particles are used to study their cyclic voltammetry (CV), electrochemical impedance spectra (EIS), Galvanostatic charge-discharge and thermal analysis.

Experimental

Materials and Methods

The materials used for the entire work with all the specifications, purity, grades, structural and chemical formulas with supplier names are mentioned in Table 2. The black mass of waste Li-ion batteries was obtained from different manufactures in Bengaluru, India. The hydrometallurgical method is adapted for the recovery of the metals like Zn, Mn, Li, Co, Ni and Cd from the waste batteries.

Materials	Specifications	Suppliers
Waste batteries	1/2AA, AAAA,AAA, AA, A C, D types	different manufactures, Bengaluru India
Oxalic acid di-hydrate $HO_2CCO_2H \cdot 2H_2O$	Molar mass: 192.16 g/mol	Merck, Bengaluru, India
Hydrogen peroxide (H_2O_2)	Molar mass: 34.01 g/mol	Merck, Bengaluru, India
Citric acid ($C_6H_8O_7$)	Molar mass: 126 g/mol	Merck, Bengaluru, India
Sulphuric acid (H_2SO_4)	Molar mass: 39.9 g/mol	Merck, Bengaluru, India
Sodium Hydroxide (NaOH)	Molar mass: 40 g/mol	Merck, Bengaluru, India
N-Methyl-2-Pyrrolidone (C_5H_9NO)	Molar mass: 99.13 g/mol	Sigma Aldrich
Sodium carbonate (Na_2CO_3)	Molar mass: 105.98 g/mol	Merck, Bengaluru, India

Table 2: Details about the chemicals used in this work

Metal Composition in Waste Lithium Ion Batteries: 10 g of active material was poured in to the 250 mL iodine flask and kept on water bath at constant temperature. The inductive coupled plasma optical emission spectroscopy (ICP-OES) was used to study the concentration of Li and Co in the above obtained mixture. After leaching, it was filtrated. The percentage recovery of metals was calculated according to the following formula (1).

$$X_B = \frac{m_1}{m_2} \times 100\% \quad (1)$$

Where XB is recovery of metal, %. m_1 is actual quality of metal leaching in gram. m_2 is metal quality of raw material in gram [49,50].

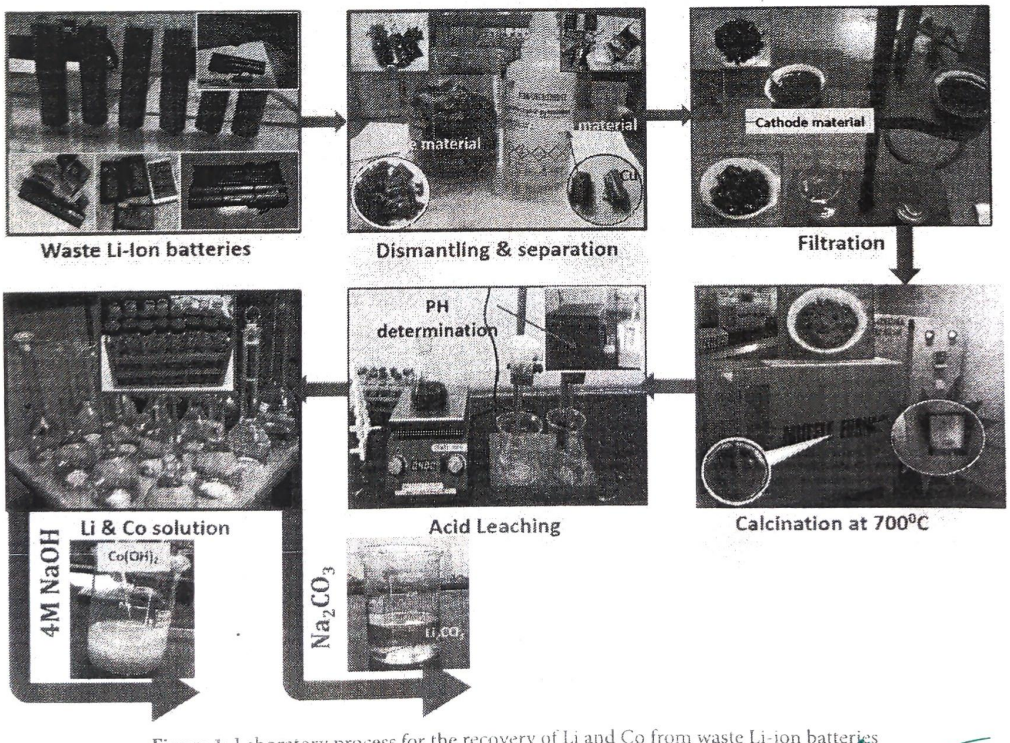

Figure 1: Laboratory process for the recovery of Li and Co from waste Li-ion batteries

Recovery of Lithium Cobalt Oxide from Battery Waste: The lithium cobalt oxide material ($LiCoO_2$) was recovered from waste lithium batteries by crushing, sieving and magnetically separation as shown in Figure 1 [51]. The thermal pre-treatment was required to remove acetylene black and Polyvinylidene fluoride (PVDF) in the active materials. The spent LIB's were dismantled manually to eliminate both the plastic and steel cases that cover the batteries. The plastic cases around the batteries were removed using a small knife and screwdriver. All steps in the experimental procedure were carried out using safety glasses, gloves and gas masks for safe operation. The anode and cathode materials were manually separated and the cathode material was treated with NMP at 100 °C for 24 hrs. After drying at 100 °C, thermal pre-treatment was necessary to eliminate graphite and PVDF in the cathode active materials. The cathode materials was calcined at 400 °C for 3 hours in a muffle and then cooled to room temperature. After roasting and cooling the cathodic material, dried the sample and obtained cathode material ($LiCoO_2$) was ground for 1hour to enable easy leaching. A measured amount of $LiCoO_2$ powder and known amount organic acids like citric acid and oxalic acid were added to the round bottom flask with constant stirring by REMI magnetic stirrer. After the leaching period, the obtained solution was filtered and washed with distilled water yielding a pink colored filtrate and a black residue for analysis.

Acid Leaching Procedure: Leaching test was conducted in a 250ml iodine flask with a mechanical stirrer, a temperature sensor and a refluxing condenser fitted to it. For each test the solution mixture was freshly prepared by dissolving the requisite amount of analytical grade oxalic acid (OA) or citric acid (CA) and washed battery powder in 100 ml of 3M H_2SO_4 solution, according to the experimental plan. During each test 1ml of leach liquor was withdrawn after 1h, 3h and 5h to measure the concentration of Li and Co by inductive optical emission spectroscopy (ICP-OES). Each sample was diluted 1:10 by an acidic solution of HNO_3 (pH~2) to avoid precipitation of metals and kept at 5 °C. After 5 hours, when reactions were stopped, pH was measured and the mixtures were filtered, washed and put in the oven at 100 °C. After 24h solid residues were recovered and weighted to evaluate the weight loss. All leaching experiments were performed at a constant stirring speed of 400 rpm. NaOH was used to precipitate Co from leach Liquor as cobalt hydroxide ($Co(OH)_2$). After the recovery cobalt the leach liquor was concentrated and treated with Na_2CO_3 to precipitate Li as lithium carbonate (Li_2CO_3). The possible leaching reaction as indicated in equation 1 (Figure 2).

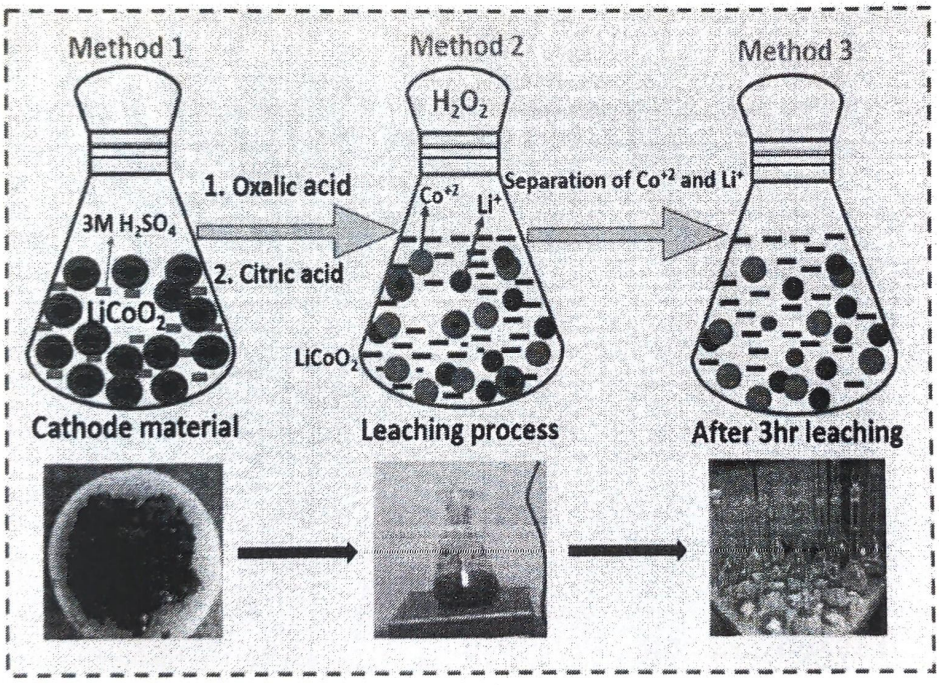

Figure 2: Possible leaching reaction process of cathode material with OA and CA leachants

Results and Discussions

X- Ray Photoelectron Spectroscopy (XPS) Studies

The valence states, composition and empirical formula of elements in the dry powder were analyzed using X- ray photoelectron spectroscopy method as shown in the Figure 3a-3f.

Figure 3b) and 3c), the peak at Li 1s = 55.6 eV, Co $2p_{3/2}$ = 781.1 eV and Co $2p_{1/2}$ = 796.4 eV corresponds to lithium and cobalt. In Figure 3d) and 3e), the peaks at the binding energy C 1s = 284.5eV and oxygen 1s = 533.1eV are confirming the presence of carbon and oxygen respectively. In Figure 3f), the binding energy 642.0 eV and 653.1 eV are attributed to manganese of $2p_{3/2}$ and $2p_{1/2}$ core level.

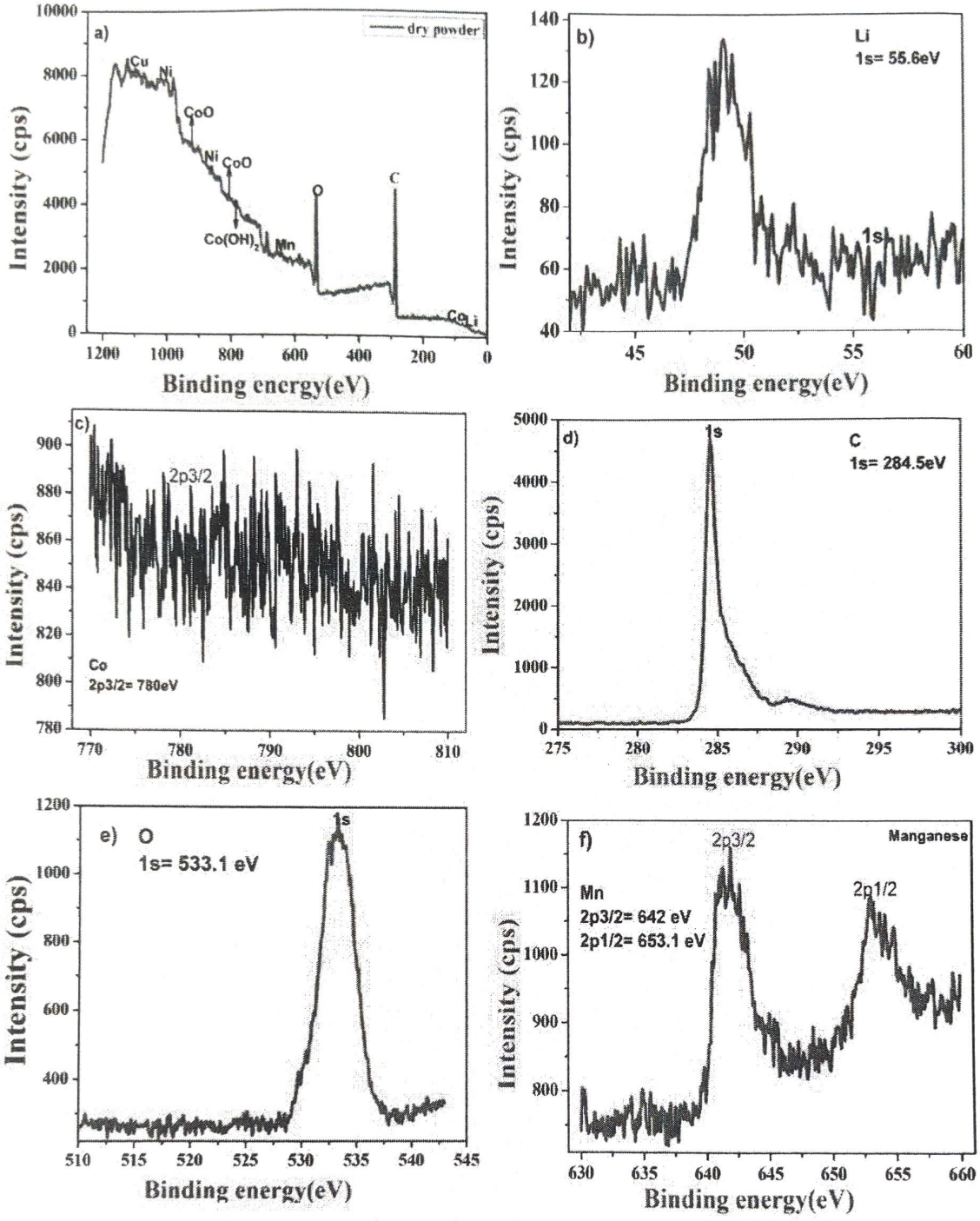

Figure 3: XPS spectra: (a) Wide angle spectrum of dry powder, (b) lithium (Li), (c) cobalt (Co), (d) carbon (C), (e) oxygen (O), (f) Manganese (Mn)

X-Ray Diffraction (XRD) Studies

The XRD of before and after treating with NMP, Li_2CO_3 and $Co(OH)_2$ were shown in Figure 4 a) to 4 b). The particle sizes of all the samples were evaluated with Scherrer's equation and also other constraints such as strain (ε), stacking fault (SF) and dislocation density (δ) calculated by the following Equations (2 to 6).

$$D = \frac{0.9\lambda}{\beta cos\theta} \tag{2}$$

Where k; constant depends on the grain shape (about 0.90), λ; the X- ray wavelength (0.15418 nm), β; the full width at half maximum (FWHM) of the diffraction line and θ; the diffraction angle.

$$\cos\theta = \varepsilon(4\sin\theta) + \frac{\lambda}{D} \tag{3}$$

The Williamson and Hall (W-H) process were suggested that when the area result and lattice micro strain effect were together simultaneously working, their mutual properties give the final line broadening FWHM which was the summation of crystallite size and lattice alteration. In Equation (2), 4sinθ and βcosθ gives straight line where ε is the strain related with obtained samples and intercept (0.90λ/D) of the line provides average crystallite size (D) and slope of line gives the strain (ε).

The values found were equivalent with the size measured from Scherrer's Equation. The occurrence of dislocations strongly affects various properties of the materials. The movement of a dislocation is hindered by new dislocations present in the sample. The greater dislocation density indicates a higher hardness of the materials and the structural parameters (δ, ε and SF) were controlled by the additional connection as indicated in Table 3 [52].

$$\delta = \frac{1}{D^2} \tag{4}$$

$$\varepsilon = \frac{\beta \cos\theta}{4} \tag{5}$$

$$SF = \frac{2\pi^2}{45\sqrt{3\tan\theta}} \tag{6}$$

Sample	FWHM (rad)	Average Crystalline Size (nm)	Strain (ε)×10^{-3}	stacking fault SF	dislocation density (δ) (10^5 lin m^{-2})
Without NMP	0.22	39.15	0.0509	0.396	6.52
With NMP	0.21	36.18	0.0535	0.522	7.67
Li_2CO_3	0.144	57.03	0.0348	0.497	3.06
$Co(OH)_2$	0.169	49.14	0.0405	0.471	4.14

Table 3: The crystallite size and other structural parameters of powder without treating with NMP, powder with NMP Li_2CO_3 and $Co(OH)_2$

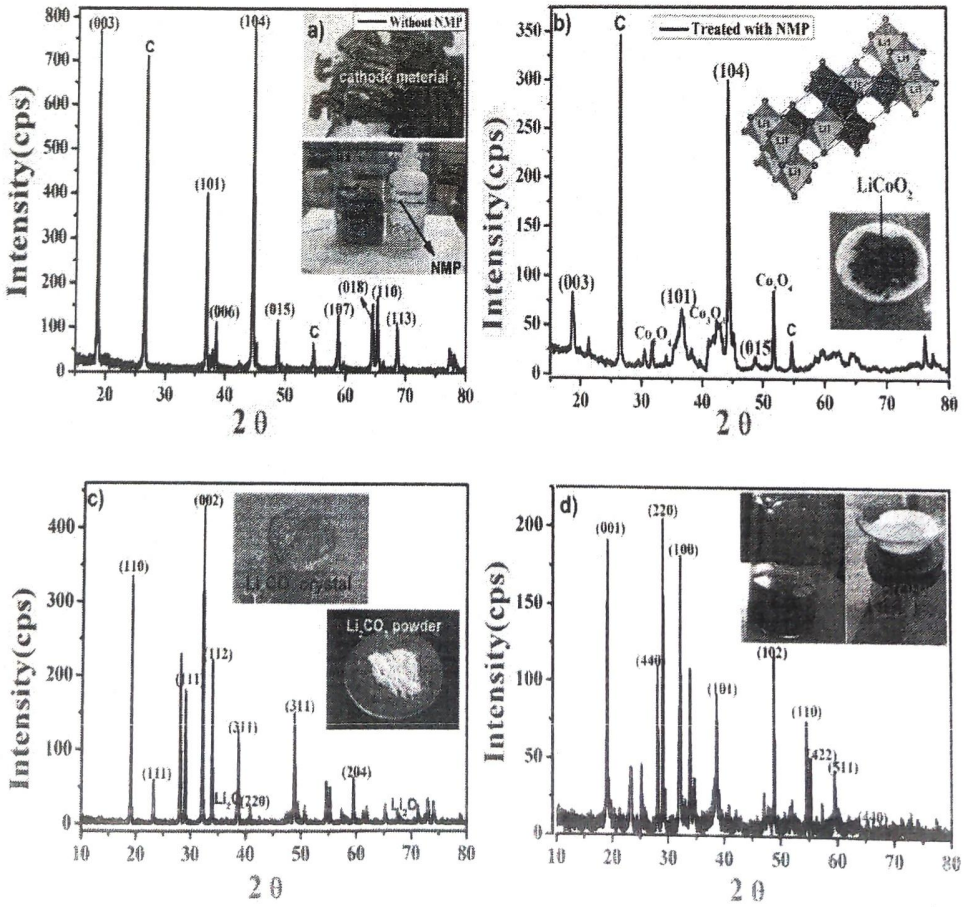

Figure 4: XRD spectrum of (a) $LiCoO_2$ without NMP, (b) $LiCoO_2$ with NMP, (c) Li_2CO_3, (d) $Co(OH)_2$

The calculated average crystallite size of cathode material without treated with NMP as well treated with NMP, La_2O_3 and $Co(OH)_2$ were found to be 34.15, 36.16,42.84 nm respectively as shown in Table 1. In the XRD of all the samples were observed to the spectra which were more intense and sharp, demonstrating excellent crystalline nature.

In Figure 4a and 4b) shows XRD patterns of the cathode material without NMP as well treated with NMP are obtained from waste LIBs and calcined at 400 °C for 5 hrs. Lithium cobalt oxide $LiCoO_2$, Co_3O_4 and carbon were main constituents present in the powder (JCPDS: 65-6232) as shown in Figure 4a and 4b).

The crystalline $LiCoO_2$ phase was clearly indicated in the XRD. The Co_3O_4 present in the active material undergoes only a transformation of the cathode material $LiCoO_2$. The appearance of Co_3O_4 is due to PVDF addition because PVDF can give out HF when heating. HF with $LiCoO_2$ to produce $HCoO_2$ and $HCoO_3$ is not stable at high temperature, it will decompose to Co_3O_4. In Figure 4b, the Co_3O_4 content get reduced because it is easy to oxidize to Co_3O_4 at higher temperature in air and at 400 °C, carbon should be minimized or removed [51-54].

The XRD pattern of La_2O_3 (JCPDS: 65-3484) and $Co(OH)_2$ (JCPDS: 74-1741) is shown in the Figure 4c and 4d. Figure 4c, the peaks at 2θ values of 24.02°, 25.7°, 29.08°, 33.4°, 38.5°, 40.88°, 48.8° and 54.6° corresponds to the crystal planes of (100), (111), (002), (102), (200), (211) and (204) of La_2O_3 nano particles. The strong and fine peak suggests that material has well crystalline nature of particles. Certain peaks of La_2O_3 lithium oxide was also identified, signifying the occurrence of traces of the metallic oxide. In Fig 4 d) the peaks at 2θ values of 24.02°, 28.06°, 29.08°, 32.06°, 38.86°, 48.82°, 54.57°, 55.52°, 59.72° and 65.36° resembles to the crystal planes of (001), (440), (220), (100), (111), (102), (110), (422), (511) and (440) of $Co(OH)_2$ nano particles.

Scanning Electron Microscopy (SEM) Studies

The SEM images of cathode material $LiCoO_2$ without treated with NMP and treated with NMP, La_2O_3 and $Co(OH)_2$ were shown in Figure 5a to 5d). In Figure 5a), the waste cathode materials before treating with NMP contained large secondary particles with irregular morphologies. In Figure 5b), the fine distributed particles can be observed and the size of $LiCoO_2$ with homogeneous and well-defined shape was observed for $LiCoO_2$ calcined at 400 °C for 5 hour as shown in the Figure 5b). These result indicating that most of the PVDF dissolved in NMP and $LiCoO_2$ particles separated. The macrostructure of La_2O_3 and $Co(OH)_2$ are shown in Figure 5c to 5d). In Figure 5c), the particles exhibit straight rod like structure. The hexagonal structure of La_2O_3 is about 10μm in size. In Figure 5d), $Co(OH)_2$ reveals an identical morphology of three dimensional (3D) multi-pods nano structures and branches are highly crystalline nature. In Figure 5d), most of the multi-pods are present more than ten pods [55-56].

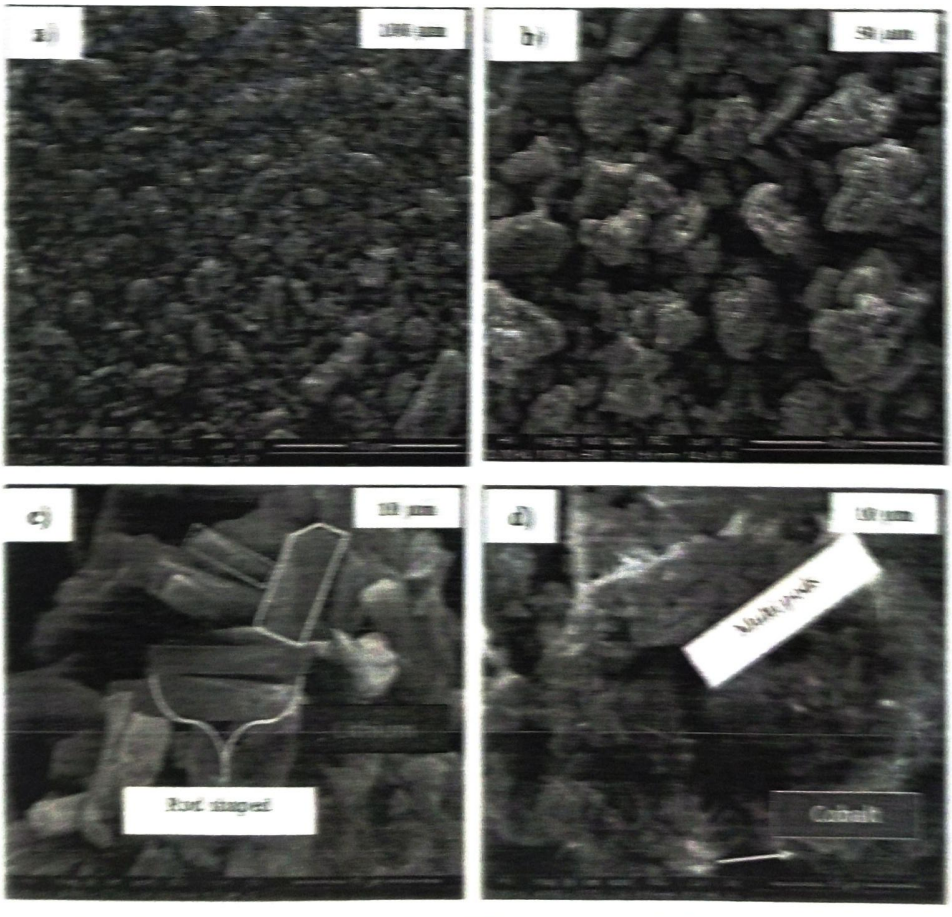

Figure 5: SEM images of a) $LiCoO_2$ without NMP b) $LiCoO_2$ with NMP c) La_2O_3 d) $Co(OH)_2$

Energy Dispersive X-Ray Analysis (EDAX)

EDAX analysis was performed for cathode material ($LiCoO_2$) without treated with NMP and treated with NMP, Li_2CO_3 and $Co(OH)_2$ were shown in Figure 6a) to 6d). In Figure 6a, the powder constitutes 40.56 wt. % of C, 18.92 wt. % of Co and 17. 07 wt. % of Ni, 15.82 wt. % of Mn with small quantity of Al, Cu, O and P were the main elements present in the powder. In Figure 6b, 93.03 wt. % of Co, 6.23 wt. % of Co with little amount of aluminium. EDAX study was the conventional solid-state analysis techniques and it does not identify lithium because of the too low energy of Li (Z = 3) K X-rays. In Figure 6c) and 6d), the Li_2CO_3 comprises 64.71 wt. % of Co, 19.32 wt. % of Oxygen, 15.97 wt. % of carbon and for $Co(OH)_2$ contains 91.79 wt. % of Co and 8.21 wt. % of oxygen.

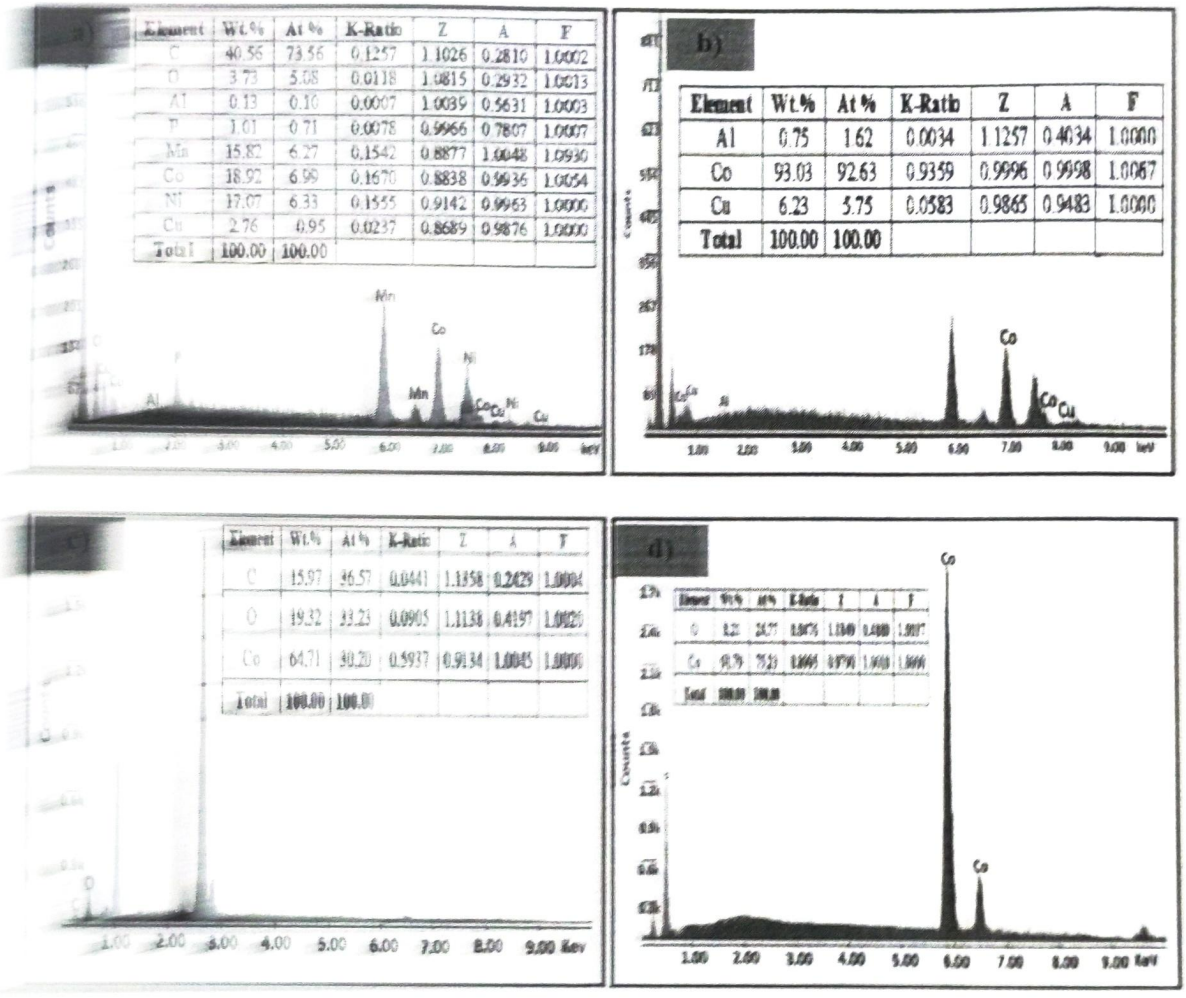

Figure 6: EDAX spectrum of (a) $LiCoO_2$ without NMP, (b) $LiCoO_2$ with NMP, (c) Li_2CO_3, (d) $Co(OH)_2$

Fourier Transforms Infra-Red Spectroscopy (FTIR) Studies

FTIR was performed for cathode material ($LiCoO_2$) without treated with NMP and treated with NMP, Li_2CO_3 and $Co(OH)_2$ which were shown in Figure 7a) to 7d). In Figure 7a, the cathode materials before and after treated with NMP were characterized by using FTIR spectrum as shown in Figure 7a) to 7b).

The cathode material before and after treated with NMP found at the wave numbers of 2317.3, 2097.7, 2006.9, 1407.4, 860.9 and 669.1 cm^{-1} after treating with NMP indicating that, PVDF is decomposed completely after heating at 400 °C for 3hrs. The band at 2317.3 cm^{-1} can be assigned to the vibration of CO_2 in the gas phase physically adsorbed on the material surface and band at 1407.4 cm^{-1} can be recognized to the bending mode of the H_2O molecule. In Figure 7c, the wave numbers found at 2340.9, 2105.5, 1435.1, 1090.5, 879.5 are the main characteristic bands of Li_2CO_3. The absorption peak at 3600cm^{-1} corresponds to O–H stretching mode of LiOH and the peak at 1600 cm^{-1} for water molecule in LiOH. Other absorptions below 1000cm^{-1} are associated with Co–O stretching and Co-OH bending vibrations. The broad peaks at low-frequency absorption 613cm^{-1} is attributed to M–O bond and FTIR spectrum of $Co(OH)_2$ sample as shown in the Figure 7d). The strong peak at 3600cm^{-1} corresponding to the free O–H group absorption frequency at 1600cm-1 is due to bending mode of the -OH group of H_2O molecule. The broad peaks at 1000–1500cm-1 is associated with Co-O stretching as well as Co-OH bending vibration [59,60].

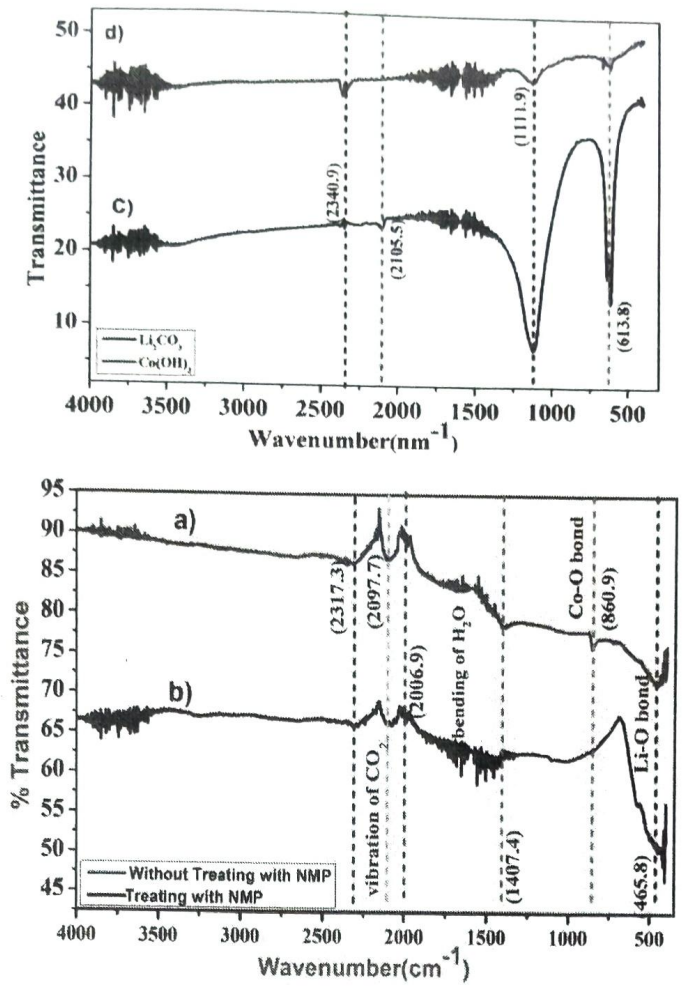

Figure 7: FTIR spectrum of (a) $LiCoO_2$ without NMP, (b) $LiCoO_2$ with NMP, (c) Li_2CO_3, (d) $Co(OH)_2$

Recovery of Li_2CO_3 and $Co(OH)_2$ from Leach Solution

The measured volume of leached solution was taken in a 500ml beaker with a slight excess of 4M NaOH which was added to the beaker with constant magnetic stirring speed (300rpm) and 30 min reaction time. The Co^{2+} ions reacts with NaOH present in the leach solution to completely precipitate as $Co(OH)_2$ nano particles. The solution was filtered using Whatmann paper 42 and the solid residue was dried at 100 °C for 24 hours. Similarly, for recovery of lithium, saturated solution of sodium carbonate with a high temperature (95 °C) was used to precipitate Li as Li_2CO_3 nano particles.

Differential Scanning Calorimetry (DSC) and TGA analysis

The Li_2CO_3 and $Co(OH)_2$ nano particles were recovered from waste leached battery solution as shown in Figure 8a) to Figure 8b). In Figure 8a demonstrate the Li_2CO_3 nano particles reveals three separate thermal decomposition steps. The initial decomposition of the weight loss at about 80 °C can be recognized to the loss H_2O molecules and the first phase weight loss occur at 278.8 °C (95.4 %) which indicating the removal of some gases like CO_2 because CO_3^{2-} based precursor accompanied by exothermic peaks can be appeared in the DSC curve in the sample.

The second decomposition curve starts at 464.18 °C (22.4 %) and the third exo-endothermic phase is around 715 °C (5.44 %) can be attributed to the melting point of Li_2CO_3 nano particles [61,62]. The mass loss between 464.18 °C and 715 °C is mainly due to the conversion of reactants into the product. The total mass loss occurs under 715 °C so it can be highlighted that the thermal stability of Li_2CO_3 recovered from waste battery is started at 460 °C [63].

In Figure 8b, the $Co(OH)_2$ nano particles shows two separate thermal decomposition steps. The initial weight loss at 63 °C can be ascribed to the elimination of water and CO_2 from the dehydroxylation and fragmentation of carbonate assemblies. The first decomposition mass loss arised at occur at 424.12 °C (95.6 %) which signifying the exclusion of certain gases like CO_2. The second exo-endothermic phase is around 632 °C (85.6 %) can be recognised to the melting point of $Co(OH)_2$ nano particles. It is noticed that both exothermic (DTA), endothermic peaks (DSC) and glass transition temperature (Tg) are recognized about 374 °C for Li_2CO_3 and 567 °C for $Co(OH)_2$ as shown in the Figure 8a) and 8b). Generally under Tg, the fragments do not have segmental motion and adjacent Tg, the fragments can start exciting. It is supposed that the increase in Tg is related to the increase in thermal

stability of the sample. The above results indicating that the recovered Li_2CO_3 and $Co(OH)_2$ from waste Li-ion batteries are more thermally stable and their excellent use full materials for energy storage applications.

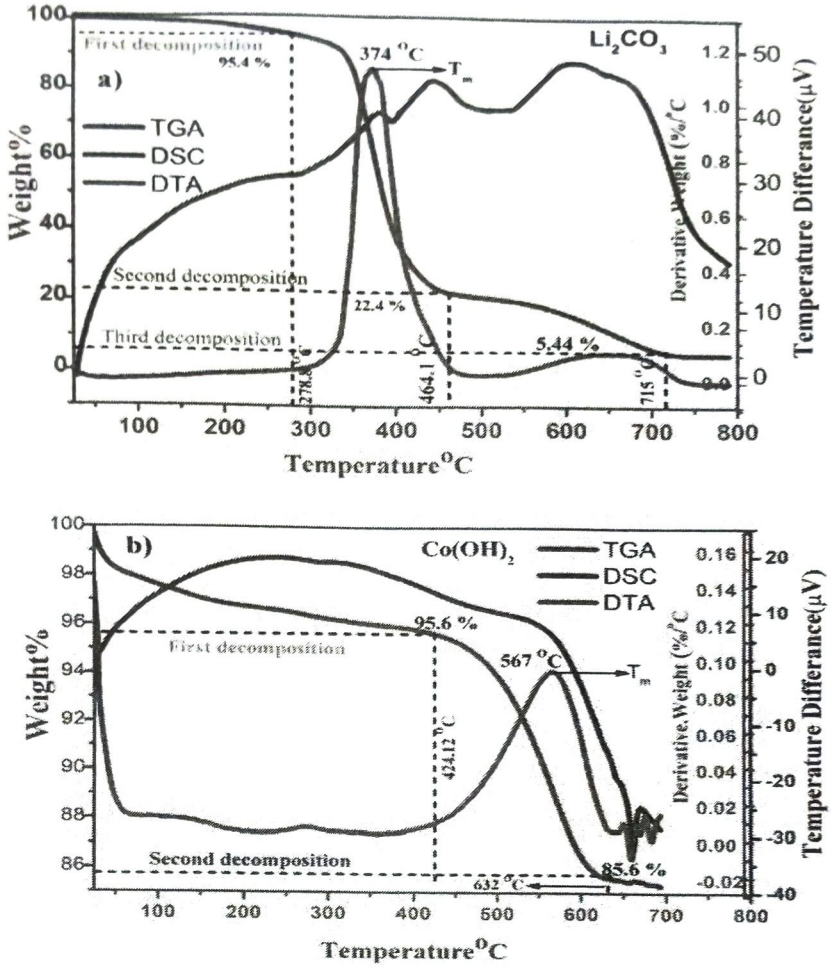

Figure 8: TGA/DSC/DTA of (a) Li_2CO_3 and (b) $Co(OH)_2$

Electrochemical Studies of Li_2CO_3 and $Co(OH)_2$

Cyclic Voltammetry (CV) Studies: CV is one of the Potentiodynamic form used for electrochemical evaluation. In an experiment of CV, the potential of working electrode is ramped versus time in linearly. To present the cyclic voltammogram outline, the obtained working electrode current is plotted against the voltage applied (i.e., potential of working electrode). The reversibility of the redox couple is more, the shape of oxidation and reduction peaks becomes exactly similar. For this reason, the CV data can make available in sequence about potentials of redox couple and rates of electrochemical reaction.

In the CV analysis, the working electrode (5% Li_2CO_3 or 5% $Co(OH)_2$) was prepared by mixing 0.025g of active material +0.475g of graphite + 3-5 drops of polytetrafluoroethylene (PTFE) solution which was added as a binder and blended by hand mixing with a mortar and pestle for about 30 min until a uniform thin sheet achieved. The obtained thin sheet was pressed on nickel mesh (area about 1 cm^2) to create a good conductivity with the Ni mesh and active material. In the same way, 10%, 15% Li_2CO_3 and 10% $Co(OH)_2$ electrodes were prepared. Finally the obtained electrode was dried at 50 °C for 48 hours and the prepared electrodes were kept for 20 days electrode setting because for stability of the electrode.

An electrochemical measurement comprises three electrode system having active material (Li_2CO_3/$Co(OH)_2$), Ag/AgCl electrode and a platinum as counter electrode. CV measurements were applied in the potential range +0.2 to -0.6V using 3M KOH as shown in the Figure 9a-c and Figure 10a-c. In Figure 9a-c, the electrochemical reversibility was calculated by seeing of the difference between the E_O and E_R at 0.01 V/s scan rate. We can report that the electrode reversibility reaction of 15% Li_2CO_3 was minimum as compared to that of 5% Li_2CO_3 and 10% Li_2CO_3 and CV curves displays a quasi-reversible electron transfer process representing that capacitive behavior was predominantly based on the redox mechanism as indicated in Table 4. The electrochemical reversibility of 10% $Co(OH)_2$ was decreased as compared to that of 5% $Co(OH)_2$ as shown in the Figure 10a-c. According to the Randles-Sevcik equation for reversible process, the height current is denoted by the Equation 7.

$$Ip = 2.69 \times 10^5 \times n^{3/2} \times A \times D^{1/2} \times C_0 \times v^{1/2} \quad (7)$$

Where n is the number of electron transferred in the reaction, the active surface area (A), diffusion co-efficient (D), scanning rate (v) and initial concentration of the chemical (C_0) respectively. The greater linear association involving in peak current (ip) and number of electron transferred ($n^{1/2}$) confirm that the electrode reaction of Li_2CO_3 and $Co(OH)_2$ were measured by hydrogen diffusion co-efficient (D). The increased D value of 15% Li_2CO_3 and 10% $Co(OH)_2$ revealed that electrochemical activity was more effective compared to that of 5% Li_2CO_3 and 10% Li_2CO_3 and 5% $Co(OH)_2$.

Sample	E_O (V) $\times 10^{-3}$	E_R (V) $\times 10^{-3}$	E_O - ER(V) $\times 10^{-3}$	D(cm^2S^{-1}) $\times 10^{-5}$	Rct (Ω)	C $\times 10^{-8}$
5 % Li2CO_3	0.105	-0.357	0.462	3.537	749.5	1.104
10 % Li2CO_3	0.269	-0.189	0.458	9.03	753.1	5.514
15 % Li2CO_3	0.059	-0.056	0.115	14.52	958.0	10.02
5 % $Co(OH)_2$	1.08	-0.128	1.208	0.698	14.3	3.085
10 % $Co(OH)_2$	0.056	-0.215	0.27	3.417	27.5	4.871

Table 4: Oxidation potential (E_O), reduction potential(E_R), the difference between E_O and E_R and diffusion co-efficient of different electrodes

Electrochemical Impedance Spectroscopy (EIS) Studies: Electrochemical impedance is usually measured by means of making use of an AC capacity to an electrochemical cell after which computing the current throughout the cell. The electrochemical impedance was measured by the use of small excitation signal and it is achieved in order that the pseudo-linear cell response. In a system of linear or pseudo-linear, the current responsible to sinusoidal potential can be a sinusoid on the similar frequency however transferred in phase. The EIS is a powerful tool for studying electron transfer between active surface and electrolyte. AC impedance was carried out for Li_2CO_3 and $Co(OH)_2$ with an ac bias voltage of 5 mV in the frequency range from 1Hz to 0.1MHz as indicated in Figure 9d and 10d. In these graphs the semi-circle seems at higher frequency region, the charge-transfer resistance (Rct) is parallel connection to double layer capacitance (C_{dl}) and Warburg impedance (W) is arised to the diffusion of ions [64]. In Figure 9d and Figure 10c-d, the charge transfer resistance (Rct) and capacitance (C) value of 15% Li_2CO_3 and 10% $Co(OH)_2$ electrode is far greater than that of other electrodes, which shows that the electrochemical reaction of electrode precedes more over other electrodes as given in Table 4.

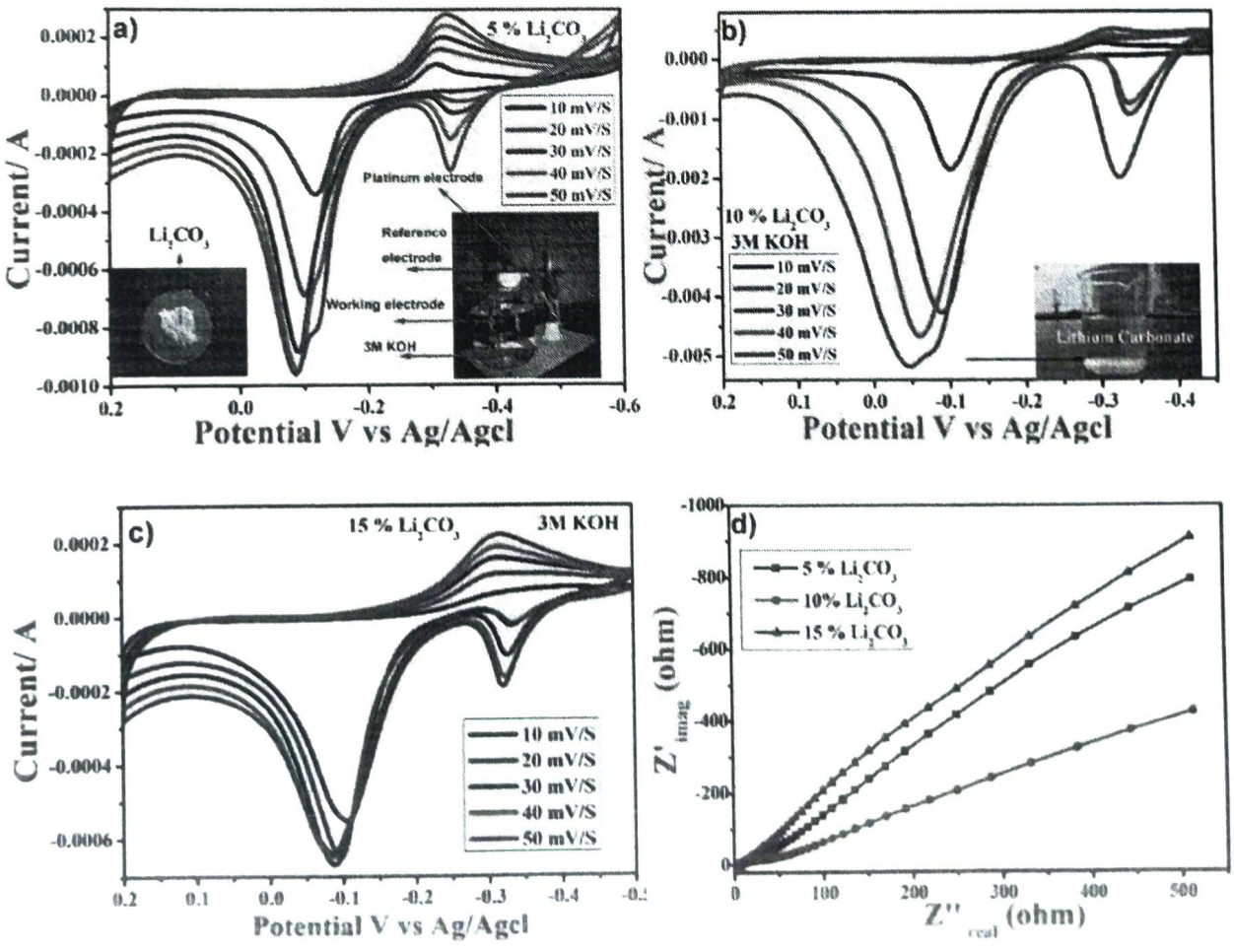

Figure 9: CV curves of (a) 5% Li_2CO_3, (b) 10% Li_2CO_3, (c) 15% Li_2CO_3, (d) Nyquist plots for 5% Li_2CO_3, 10% Li_2CO_3 15% Li_2CO_3 using 3M KOH solutions

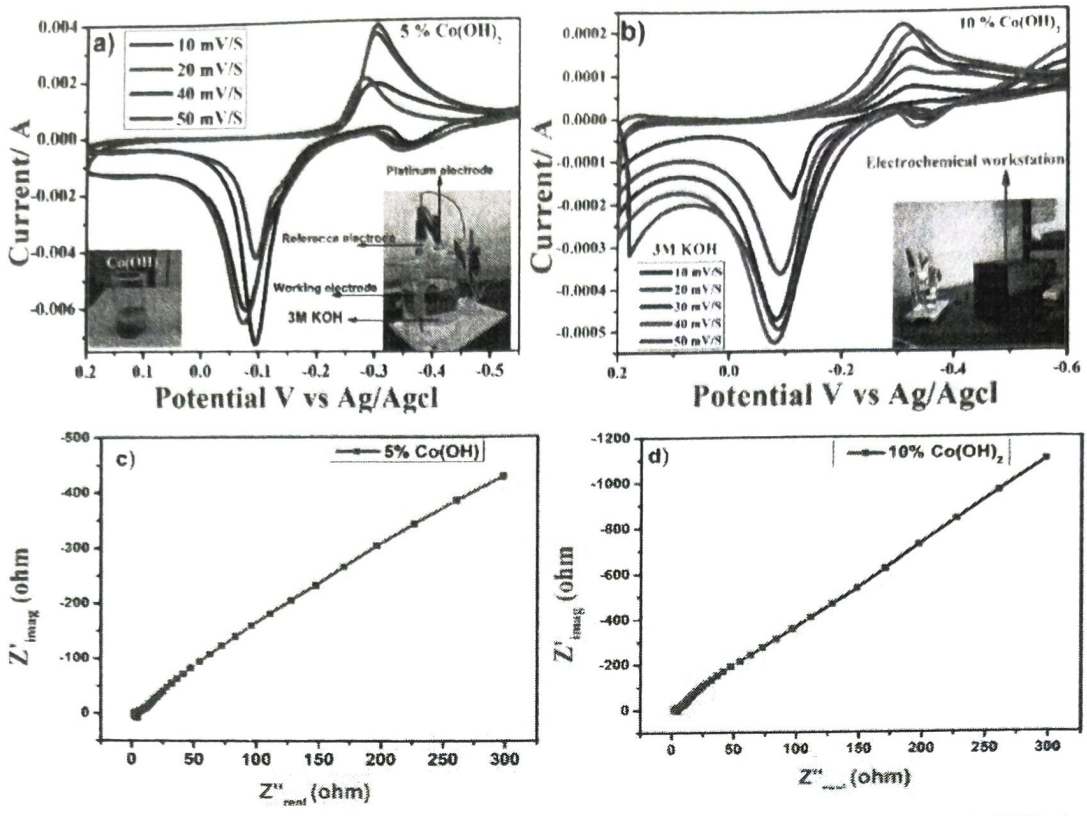

Figure 10: CV curves of (a) % $Co(OH)_2$, (b) 10% $Co(OH)_2$, (c) Nyquist plots for 5% $Co(OH)_2$, d) 10% $Co(OH)_2$ using 3M KOH solution

Galvanostatic Charge-Discharge Analysis (GCD): The recovered Li_2CO_3 from leach solution was used as working electrode using 3M KOH solution as the electrolyte, Ag/AgCl as the reference electrode and platinum wire used as the counter electrode in a three electrode configuration system. The working electrode (5% Li_2CO_3) was prepared by mixing 0.025g of active material +0.475g of graphite +3-5 drops of PTFE and in the same way, 5% $Co(OH)_2$, 10% $Co(OH)_2$ and 15% $Co(OH)_2$ were prepared. The suspended solution was coated on to nickel mesh with area 1cm². Finally the obtained electrodes were dried at 50 °C for 48hrs. The galvanostatic charge-discharge (GCD) curves for 5% Li_2CO_3, 10% Li_2CO_3, 15% Li_2CO_3 and 5% $Co(OH)_2$, 10% $Co(OH)_2$ and 15% $Co(OH)_2$ were shown in Figure 10a-c and Figure 11a-c.Within the potential window of -0.6 to 0.6 V vs. Ag/AgCl. The specific capacitance (Cs) of Li_2CO_3 and $Co(OH)_2$ electrode was calculated by the following Equation (8).

$$C = \frac{I\Delta t}{m\Delta V} \tag{8}$$

Where, I is the current, ΔV is the potential window, Δt is the time of a discharge cycle and m is the mass of active material. In Figure 11a-c, the specific capacitance values of were calculated and found to be 138.4Fg^{-1}, 189.4Fg^{-1} and 2631Fg^{-1}. Likewise, in Figure 11a-c the specific capacitance values of 5% $Co(OH)_2$, 10% $Co(OH)_2$ and 15% $Co(OH)_2$ were found to be 147.9Fg^{-1}, 150.1v and 2133.8 Fg^{-1} respectively. The specific energy density (E) and power density (P) can be calculated from the GCD curve by Equation (9 and 10).

$$E = \frac{1}{2} C_S V^2 \tag{9}$$

$$P = \frac{E}{\Delta t} \tag{10}$$

Where E is the energy density, Cs is the capacitance, V is the potential window; P is the power density and Δt is the discharging time.

The specific energy density of the 5% Li_2CO_3, 10% Li_2CO_3 and 15% Li_2CO_3 were 19.6whkg^{-1}, 26.8whkg^{-1} and 412.5whkg^{-1} and the specific power density were found to be 15.9wkg^{-1}, 10.63wkg^{-1} and 3.87wkg^{-1}. Also, energy density of 5% $Co(OH)_2$, 10% $Co(OH)_2$ and 15% $Co(OH)_2$ were seemed 0.207 whkg^{-1}, 0.186 whkg^{-1} and 467.3whkg^{-1} and power density were found to be 0.295wkg^{-1}, 0.183wkg^{-1} and 14.29wkg^{-1} respectively as indicated in the Table 5 [65,66]. The above outcomes showed that the charge-discharge curves display well-symmetry and linear deviations with change of the time indicating superior capacitance and cycle performance of Li_2CO_3 and $Co(OH)_2$. This is predominantly because of the electrode reversible reaction and also revealed that as a kind of super capacitor electrode materials. The recovered Li_2CO_3 and $Co(OH)_2$ electrode materials from battery waste showing the highest specific capacitance with excellent rate capability and outstanding cycling stability (Figure 12).

Electrode	Specific Capacity (Fg^{-1})	Energy density ($whkg^{-1}$)	Power density (wkg^{-1})
5% Li_2CO_3	138.4	19.6	15.93
10% Li_2CO_3	189.4	26.8	10.63
15% Li_2CO_3	2631	412.5	3.87
5% $Co(OH)_2$	147.9	0.207	0.295
10% $Co(OH)_2$	150.01	0.186	0.183
15% $Co(OH)_2$	2133.8	467.3	14.29

Table 5: The specific capacitance, Energy and power density values of Li_2CO_3 and $Co(OH)_2$

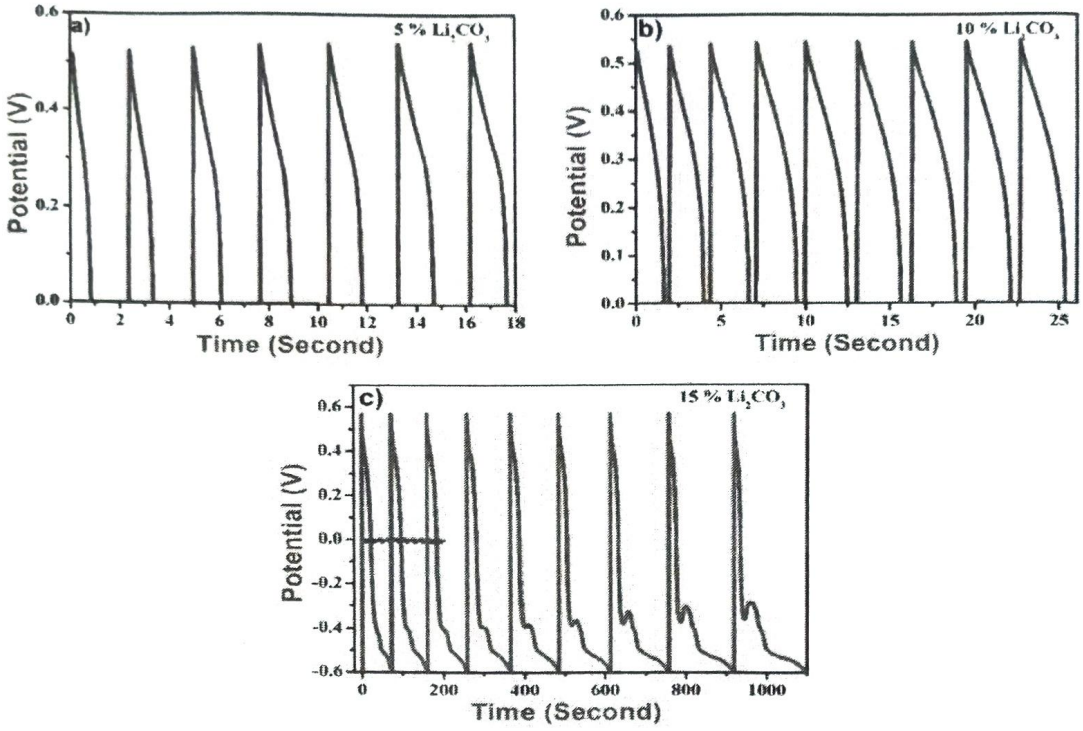

Figure 11:Charge-discharge curve (20 segments) of (a) 5% Li2CO_3, (b) 10% Li_2CO_3, (c) 10% Li_2CO_3

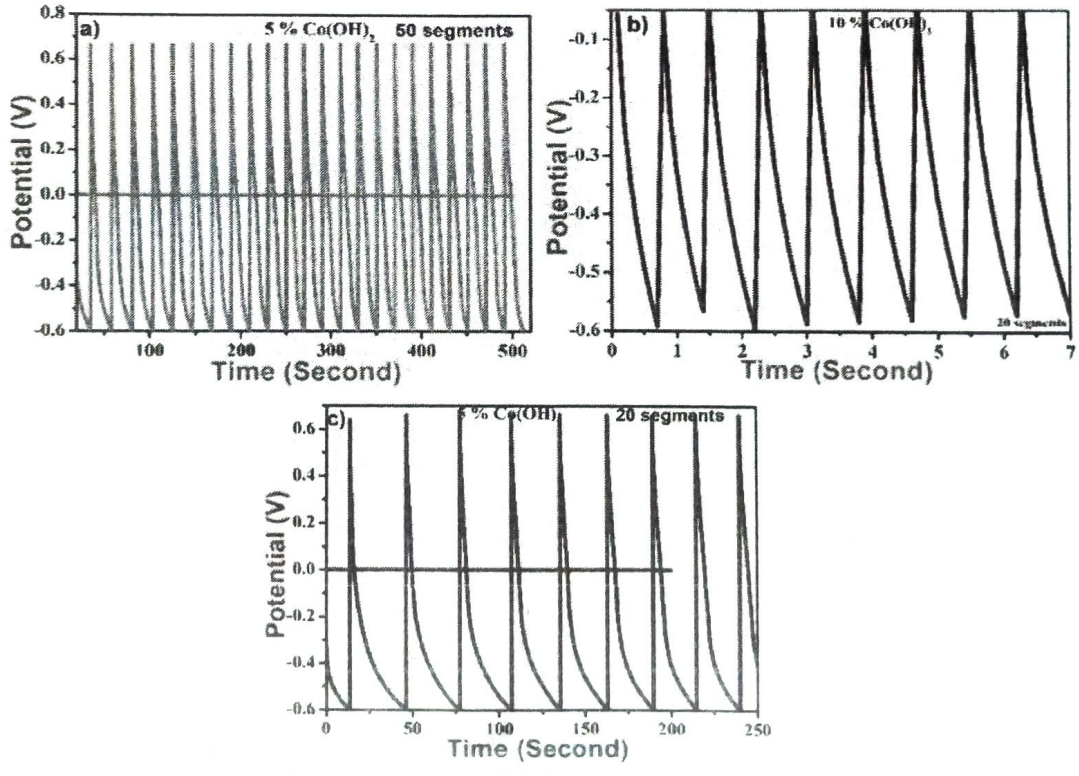

Figure 12: Charge-discharge curve of (a) 5% $Co(OH)_2$ for, (b) 5 % $Co(OH)_2$ for 50 segments, (c) 10% $Co(OH)_2$, (d) 15% $Co(OH)_2$

Conclusion

The average crystalline sizes of $LiCoO_2$ without treated NMP, treated with NMP, Li_2CO_3 and $Co(OH)_2$ were found to be 39.15, 36.18,57.03 and 49.14 nm respectively. From SEM study Li_2CO_3 and $Co(OH)_2$ particles have rod like and multi pod structures and the recoverd materials were thermally stable up to 715 °C to 632 °C. From electrochemical properties, the extreme specific capacitance of Li_2CO_3 and $Co(OH)_2$ was found to be 2631 Fg^{-1} and 2133.8 Fg^{-1}. These results confirmed that a high energy density battery can store lots of energy and a high power density battery will charge faster than a low power density battery. The charge-discharge curves display well-symmetry and linear deviations with change of the time indicating superior capacitance and cycle performance of Li_2CO_3 and $Co(OH)_2$.

References

1. Chen X, Chen Y, Zhou T, Liu D, Hu H, et al. (2015) Hydrometallurgical recovery of metal values from sulfuric acid leaching liquor of spent lithium-ion batteries. Waste Manage 38: 349-56.

2. Nayaka GP, Manjanna J, Pai KV, Vadavi R et al. (2015) Recovery of valuable metal ions from the spent lithium-ion battery using aqueous mixture of mild organic acids as alternative to mineral acids. Hydrometallurgy 151: 73- 7.

3. Pananelli F, Moscradini E (2014) Acid reducing leaching of cathodic powder from spent lithium ion batteries: Glucose oxidative pathways and particle area evolution. J indust Eng chem 20: 3201-7.

4. Castillo S, Ansart F, Laberty-Robert C, Portal (2002) Advances in the recovering of spent lithium battery compounds. JJ Power Sources 112: 247-54.

5. Contestabile M, Panero S, Scrosati B (2001) A laboratory-scale lithium-ion battery recycling process. J Power Sources 92: 65-9.

6. Zhang P, Yokoyama T, Itabashi O, Wakui Y, Suzuki TM, et al. (1998) Hydrometallurgical Process for Recovery of Metal Values from Spent Nickel-Metal Hydride Secondary Batteries. Hydrometallurgy 50: 61-75.

7. Spencer CM, Houpt TA (2001) Dynamics of c-fos and ICER mRNA expression in rat forebrain following lithium chloride injection. Molecular Brain Res 93: 113-26.

8. Mylarappa M, Venkata Lakshmi V (2018) Cyclic Voltammetry, Impedance and Thermal Properties of $CoFe_2O_4$ Obtained from Waste Li-Ion Batteries. Materials Today: Proceed 5: 22425-32.

9. Aslan A, Salur E, Gunes A, OS Sahin, HB Karadag, et al. (2019) The mechanical properties of composite materials recycled from waste metallic chips under different pressures. Int J Environ Sci Technol 16: 5259-66.

10. Aslan A, Gunes A, Salur E (2018) Mechanical properties and microstructure of composites produced by recycling metal chips. Int J Miner Metall Mater 25: 1070-9.

11. Shin SM, Kim NH, Sohn JS, Yang DH, Kim YH (2005) Development of a Metal Recovery Process from Li-Ion Battery Wastes. Hydrometallurgy 79: 172-81.

12. Kang J, Sohn G, Chang H, Senanayake G (2010) Preparation of cobalt oxide from concentrated cathode material of spent lithium ion batteries by hydrometallurgical method. Adv Power Techno 21: 175-9.

13. Shin SM, Kim NH, Sohn JS, Yang DH, Kim YH (2005) Development of a Metal Recovery Process from Li-Ion Battery Wastes. Hydrometallurgy 79: 172-81.

14. Espinosa DCR, Bernardes AMJ (2004) an overview on the current processes for the recycling of batteries. Power Sources 135: 311-9.

15. Li L, Ge J, Chen R, Wu F, Chen S (2010) Environmental friendly leaching reagent for cobalt and lithium recovery from spent lithium-ion batteries. Waste Manage 30: 2615-21.

16. Lupi C, Pasquali M, Dell Era A (2005) Nickel and cobalt recycling from lithium-ion batteries by electrochemical processes.Waste Manage 25: 215-20.

17. Swain B, Jeong J, Lee JC, Lee GH (2007) Hydrometallurgical process for recovery of cobalt from waste cathodic active material generated during manufacturing of lithium ion batteries. J Power Sources 167: 536-44.

18. Lupi C, Pasquali M (2003) Electrolytic nickel recovery from lithium-ion batteries. Miner Eng 16: 537-42.

19. Nan J, Han D, Yang M, Cui M (2006) Recovery of metal values from a mixture of spent lithium-ion batteries and nickel-metal hydride batteries. Hydrometallurgy 84: 75-80.

20. Lee CK, Rhee K (2003) Reductive leaching of cathodic active materials from lithium ion battery wastes. Hydrometallurgy 68: 5-10.

21. Lee CK, Rhee K (2002) Preparation of LiCoO2 from spent lithium-ion batteries. J Power Sources 109: 17-21.

22. Jha M K, Kumari A, Jha A K. (2013) Recovery of lithium and cobalt from waste lithium ion batteries of mobile phone. waste Manage 33: 1890-7.

23. Dakora FD, Phillips DA (2002) Root Exudates as Mediators of Mineral Acquisition in Low-Nutrient Environments. Plant Soil 245: 35-47.

24. Jones DL, Darrah PR (1994) Role of root derived organic acids in the mobilization of nutrients from the rhizosphere. Plant Soil 166: 247-57.

25. Ryan PR, Delhaize E, Jones DL (2001) Function and Mechanism of Organic Anion Exudation from Plant Roots. Plant Mol Bio 52: 527-60.

26. Strom L, Owen (2005) Organic Acid Behaviour In A Calcareous Soil Implications for Rhizosphere Nutrient Cycling. AG Soil Bio Biochem 37: 2046-54.

27. Mylarappa M, Venkata Lakshmi V, Vishnu Mahesh KR, Kantharaju S Sreenivasa S (2018) Effect of Oxalic Acid and Citric Acid on Recovery of Ni and Cd from Waste Batteries: Electrochemical and Thermal Investigation of $Ni(OH)_2$ Obtained from Leach Solution. Res J Chem Environ 22: 1-15.

28. Shen Y, Xue W (2008) Recovery of Co(II) and Ni(II) from hydrochloric acid solution of alloy scrap Trans. Nonferrous Met Soc China 18: 1262-8.

29. Pranolo Y, Zhang W, Cheng CY (2010) Recovery of metals from spent lithium-ion battery leach solutions with a mixed solvent extractant system. Hydrometallurgy 102: 37-42.

30. Provazi K, Campos BA, Espinosa DCR (2011) Recovery of Metals from Electronic Waste by Physical and Chemical Recycling Processes. Waste Manage 2: 3159 64.

31. Zhao JM, Shen XY, Deng FL, Wang FC, Wu Y (2011) Synergistic extraction and separation of valuable metals from waste cathodic material of lithium ion batteries using Cyanex272 and PC 88A. Sep Purif Technol 78: 345-51.

32. Castillo S, Ansart F, Laberty-Robert CJ (2002) Advances in the recovering of spent lithium battery compounds. Power Sources 112: 247-54.

33. Contestabile M, Panero S, Scrosati B (2001) A laboratory-scale lithium-ion battery recycling process. J Power Sources 92: 65-9.

34. Kang J, Senanayake G, Sohn J (2010) Recovery of cobalt sulfate from spent lithium ion batteries by reductive leaching and solvent extraction with Cyanex 272. Hydrometallurgy 100: 168-71.

35. Wang, Lin Y, Wu S (2009) Hydrometallurgical Recovery of Value Metals from Spent Lithium Ion Batteries. Hydrometallurgy 99: 194-201.

36. Dorella G, Mansur MB (2007) Leaching study of spent Li-ion batteries. J Power Sources 170: 210-5.

37. Li J, Shi P, Wang Z, Chen Y, Chang C (2009) A combined recovery process of metals in spent lithium-ion batteries. Chemosphere 77: 1132-6.

38. Chen L, Tang X, Zhang Y, Li L, Zeng Z (2011) Process for the recovery of cobalt oxalate from spent lithium-ion batteries. Hydrometallurgy 108: 80-6.

39. Lupi C, Pasquali M, Dell'Era A (2005) Nickel and cobalt recycling from lithium-ion batteries by electrochemical processes. Waste Manage 25: 215-20.

40. Sayed M, Badawy AA, Nayl RA, El-Khateeb MA (2014) Cobalt separation from waste mobile phone batteries using selective precipitation and chelating resin. J Mater Cycles Waste Manage 2014: 739-46.

41. Mishra D, Kim DJ, Ralph DE, Ahn JG (2008) Bioleaching of metals from spent lithium ion secondary batteries using Acidithiobacillus ferrooxidans. Waste Manage 28: 333-8.

42. Zhang P, Yokoyama T, Itabashi O, Suzuki TM (1998) Precipitation–stripping processes for heavy metal. Hydrometallurgy 47: 259-71.

43. Li L, Ge J, Wu F, Chen R, Chen S, et al. (2010) Recovery of cobalt and lithium from spent lithium ion batteries using organic citric acid as leachant. J Hazard Mater 176: 288-93.

44. Shin SM, Kim NH, Sohn JS, Dong HY, Young HK (2005) Development of a metal recovery process from Li-ion battery wastes. Hydrometallurgy 79: 172-81.

45. Mantuano DP, Dorella G, Renata CAE, Marcelo BM (2006) Analysis of a hydrometallurgical route to recover base metals from spent rechargeable batteries by liquid–liquid extraction with Cyanex 272. Power Sources 159: 1510-8.

46. Xin BP, Zhang D, Zhang X, Feng W, Li L (2009) Bioleaching mechanism of Co and Li from spent lithiumion battery by the mixed culture of acidophilic sulfur oxidizing and iron-oxidizing bacteria. Bioresour Technol 100: 6163-9.

47. Yoo KK, Shin SM, Yang DH (2010) Biological treatment of wastewater produced during recycling of spent lithium primary battery. Miner Eng 23: 219-24.

48. Sonmez MS, Kumar RV (2009) Leaching of waste battery paste components. Part 1: Lead citrate synthesis from PbO and PbO_2. Hydrometallurgy 95: 53-60.

49. Wang J, Chen M, Chen H, Luo T, Xu Z (2012) Leaching study of spent Li-ion batteries. Procedia Environ Sci 16: 443-50.

50. Li Li, Jing Ge, Chen R, Wua F, Chen S, et al (2010) Environmental friendly leaching reagent for cobalt and lithium recovery from spent lithium-ion batteries. Waste Manage 30: 2615-21.

51. Li Li, Dunn JB, Zhang XX, Gaines L, Chen RJ, et al (2013) Recovery of metals from spent lithium-ion batteries with organic acids as leaching reagents and environmental assessment. J Power Sources 233: 180-9.

52. Mylarappa M, Venkata Lakshmi V, Vishnu Mahesh KR, Nagaswarupa HP, Raghavendra N (2017) Synthesis and characterization of Mn-$ZnFe_2O_4$ and Mn-$ZnFe_2O_4$/rGO nanocomposites from waste batteries for photocatalytic, electrochemical and thermal studies. Mater Res Express 4: 115603.

53. Liang Chen, Xincun Tang, Yang Zhang, Lianxing Li, Zhiwen Zeng, et al (2011) Process for the recovery of cobalt oxalate from spent lithium-ion batteries. Hydrometallurgy 108: 80-6.

54. Li Li, Zhai L, Zhang XX, Jun L, Renjie C, et al. (2014) Recovery of valuable metals from spent lithium-ion batteries by ultrasonic-assisted leaching process. J Power Sources 262: 380-5.

55. Covarrubias C, Duran JP, Maureira M (2018) Facile synthesis of lithium carbonate nanoparticles with potential properties for bone repair applications. Mater Lett 219: 205-8.

56. Shao L, Ma R, Wu K, Shui M, Lao M, et al. (2013) Metal carbonates as anode materials for lithium ion batteries. J Alloys Compd 581: 602-9.

57. Pen Chen, Li Gub, Xuebo Cao (2010) From single ZnO multipods to heterostructured ZnO/ZnS, ZnO/ZnSe, ZnO/Bi2S3 and ZnO/Cu2S multipods: controlled synthesis and tunable optical and photoelectrochemical properties. Cryt Eng Comm 12: 3950-8.

58. Nethravathi C, Catherine R, Sanjay S, Rajamathi, Claudia F (2017) High coercivity stellated cobalt metal multipods through solvothermal reduction of cobalt hydroxide nanosheets. RSC Adv 7: 1413.

59. Ray LF, Kloprogge JT (1999) Infrared emission spectroscopic study of brucite. Spectrochim Acta Part A: Mol Biomol Spectr 55: 2195-205.

60. Sang WK, Bob JK, Jeong HP, Hur MG, Yang SD, et al. (2010) γ-ray Radiation Induced Synthesis and Characterization of α -Cobalt Hydroxide Nanoparticle. Korean Chem Soc 31: 910-4.

61. Oberhofer M, Scharmann A (1981) Applied thermoluminescence dosimetry. Published for the Commission of the European Communities 108.

62. Oberhofer M, Scharmann A (1993) Techniques and management of personnel thermoluminescence dosimetry services. Kluwer academic publishers, London.

63. Manteghi F, Kazemi SH, Peyvandipoor M, Ahmad A (2015) Preparation and application of cobalt oxide nanostructures as electrode materials for electrochemical supercapacitors. RSC Adv 93: 75838-6665.

64. Mylarappa M, Venkata Lakshmi V, Vishnu Mahesh KR, Kantharaju S (2018) Effect of Oxalic Acid and Citric Acid on Recovery of Ni and Cd from Waste Batteries: Electrochemical and Thermal Investigation of Ni $(OH)_2$ Obtained from Leach Solution. RJCE 22: 1:15.

65. Barbieri EMS, Lima EPC, Cantarino SJ, Lelis MFF, MBJG Freitas (2014) Recycling of spent ion-lithium batteries as cobalt hydroxide, and cobalt oxide films formed under a conductive glass substrate, and their electrochemical properties. J Power Sources 269: 158-63.

66. Yanan Xu, Wang X, An C, Wang Y, Jiao L, et al. (2014) Facile synthesis route of porous $MnCo_2O_4$ and $CoMn_2O_4$ nanowires and their excellent electrochemical properties in supercapacitors. J Mat Chem A 2: 16480-8.